Received: 30 March 2020 | Revised: 13 October 2020 | Accepted: 13 October 2020

DOI: 10.1002/nme.6579

RESEARCH ARTICLE

WILEY

Computing the effective response of heterogeneous materials with thermomechanically coupled constituents by an implicit fast Fourier transform-based approach

Daniel Wicht | **Matti Schneider** | **Thomas Böhlke**

Karlsruhe Institute of Technology (KIT), Institute of Engineering Mechanics, Karlsruhe, Germany

Correspondence
Thomas Böhlke, Karlsruhe Institute of Technology (KIT), Institute of Engineering Mechanics, Karlsruhe, Germany.
Email: thomas.boehlke@kit.edu

Funding information
Deutsche Forschungsgemeinschaft, Grant/Award Numbers: BO 1466/12- 2, GRK 2078

Abstract

Thermomechanical couplings are present in many materials and should therefore be considered in multiscale approaches. Specific cases of thermomechanical behavior are the isothermal and the adiabatic regime, in which the behavior of real materials differs. Based on the consistent asymptotic homogenization framework for thermomechanically coupled generalized standard materials, the present work is devoted to computing the effective thermomechanical behavior of composite materials in the context of fast Fourier transform (FFT)-based micromechanics. Exploiting the homogeneity of the temperature on the microscale, we develop a fast implicit staggered solution scheme for the coupled problem, which is compatible to existing strain-based micromechanics solvers. Due to its implicit formulation, the algorithm permits large time steps for computations involving strong thermomechanical coupling. We investigate the performance of modern FFT-based algorithms combined with the proposed thermomechanical solution strategy. In this context, the Barzilai–Borwein method is identified as particularly efficient, inducing only a small overhead compared with the traditional isothermal setting. We demonstrate the effectiveness of the presented approach for short-fiber reinforced composites with viscoelastic matrix behavior.

KEYWORDS

composites, FFT-based micromechanics, homogenization, thermomechanical coupling, viscoelasticity

1 | INTRODUCTION

When subjected to a wide range of thermomechanical loadings, the interplay between temperature and deformation fields has a significant impact on the effective behavior of structural materials. Clearly, variations in temperature lead to changes in the mechanical behavior, for example, in the form of thermal softening. In return, mechanical loadings can induce temperature changes, due to internal dissipation or changes in entropy. This interplay of mechanical and thermal effects is governed by the balance equations for linear momentum and internal energy (in terms of the heat equation). For instance, in the vicinity of their glass transition temperature polymers are particularly sensitive to temperature variations.[1] Especially when subjected to cyclic loading, self-heating due to dissipation can critically affect the mechanical properties of materials and the life time of components, see, for example, Rittel,[2] Mortazavian-Fatemi,[3] or Katunin.[4]

Thus, for the optimal use of materials, characterizing and predicting their thermomechanical behavior is of central importance. For composite materials, this proves to be a challenging task as their properties rest on their individual constituents and microstructure. In a small-strain framework, Chatzigeorgiou et al.[5] used an asymptotic homogenization approach to derive the governing thermomechanical equations on the micro- and macroscale for generalized standard materials,[6] taking into account both the microstructure and the thermomechanical material behavior. This generalized previous studies using asymptotic approaches, for example, by Terada et al.[7] for porothermoelasticity or Temizer[8] for finite thermoelasticity. A recent review on the homogenization of dissipative materials was given by Charalambakis et al.[9]

A particular result of the asymptotic homogenization is that the microscopic balance of linear momentum depends only on the *macroscopic* temperature and is independent of temperature fluctuations on the microscale.[5] In contrast to earlier works on the homogenization of thermomechanical material properties, for example, by Willis,[10] the uniform temperature on the microscale is not an ad hoc assumption but arises as a direct consequence of first-order homogenization. As a result, the thermomechanical problem on the microscale may be solved for a homogeneous temperature and is decoupled from microscopic heat-conduction. Based on these results, Tikkarrouchine et al.[11] homogenized unidirectional short-fiber structures with temperature-independent material parameters in the context of concurrent multiscale simulations, using the finite element (FE)-software ABAQUS. Similar FE-based multiscale studies which still consider thermal conduction on the microscale were carried out by Özdemir et al.[12] for elastoplasticity and Li et al.[13] for single-crystal elastoviscoplasticity.

Motivated by the aforementioned studies, we consider solvers based on the fast Fourier transform (FFT) for the computational homogenization of thermomechanically coupled materials on the microscale. Since the pioneering work of Moulinec–Suquet,[14] these algorithms have become a well-established tool in computational micromechanics, owing to three major advantages. First, FFT-based solvers operate on a regular grid, enabling them to handle complex microstructures and making them directly compatible to modern volumetric imaging techniques such as microcomputed X-ray tomography. Second, in contrast to traditional FE-based solvers, the FFT-based methods come with a natural matrix-free implementation. This is especially relevant for finely discretized complex microstructures, where memory can become a limiting factor. Last but not least, FFT-based methods have proven to be computationally efficient, typically outperforming traditional FE-based solvers.[15-17] Indeed, FFT-based methods profit from optimized and freely available implementations of the eponymous FFT.[18] Furthermore, research effort was devoted to developing fast solution algorithms, which improve upon the performance of Moulinec–Suquet's basic iterative scheme. Currently, the most efficient families of solution schemes are the polarization-based methods,[19-21] inexact Newton methods[22,23] and quasi-Newton methods.[24-26] An overview of the advantages of these methods is provided in Appendix A. Comparative studies on the performance of various FFT-based solvers were carried out, for instance, by Mishra et al.[27] or Schneider.[25]

FFT-based methods have found widespread application in various fields, such as fracture mechanics,[28,29] interface damage,[30] and gradient plasticity,[31] as well as coupled problems such as electromechanics[32] and recrystallization kinetics.[33] In the context of thermomechanics, FFT-based methods have been used to homogenize linear thermoelastic materials[34-36] and linear thermomagnetoelectroelastic[37] materials. Shantraj et al.[38] proposed a FFT-based staggered algorithm for coupled multiphysics problems, taking thermal conduction on the microscale into account.

To exploit the power of FFT-based methods for computing the effective thermomechanical behavior of nonlinear dissipative materials, we rely upon the framework of asymptotic homogenization, as pioneered by Chatzigeorgiou et al.[5] Due to the weak coupling of mechanics and thermal conduction, the cell problem on the microscale is governed only by the microscopic balance of linear momentum and the evolution of the macroscopic temperature, cf. Section 2. Based on these results, we propose a staggered solution algorithm, where strain-field and temperature are updated in an alternating fashion, cf. Section 3. The proposed solution scheme may be applied on top of any iterative strain-based solution method and can be easily integrated into existing FFT-based computational micromechanics codes. Owing to the homogeneity of the temperature on the microscale, the temperature update only involves solving a scalar equation and introduces little overhead. The usefulness of the approach is demonstrated in Section 4 for glass–fiber reinforced polypropylene composites with strong thermomechanical coupling.

2 | FIRST-ORDER HOMOGENIZATION OF THERMOMECHANICAL COMPOSITES

Chatzigeorgiou et al.[5] introduced a framework for the asymptotic homogenization of thermomechanically coupled generalized standard materials in the quasi-static small-strain setting. As a result, they obtained governing equations for

macro- and microscale. In the following, we review the equations relevant for solving the thermomechanical cell problem on the microscopic level.

Let $Y \subseteq \mathbb{R}^d$ be a rectangular cell, with microscopic point $x \in Y$ and $d \in \{1, 2, 3\}$ spatial dimensions. We denote by $\mathrm{Sym}(d)$ the space of symmetric $d \times d$ matrices. For the following discussion, we consider the displacement fluctuation field $u : Y \times [0, T] \to \mathbb{R}^d$, the infinitesimal strain field $\varepsilon : Y \times [0, T] \to \mathrm{Sym}(d)$, the stress field $\sigma : Y \times [0, T] \to \mathrm{Sym}(d)$, the heat flux $q : Y \times [0, T] \to \mathbb{R}^d$, the entropy density $s : Y \times [0, T] \to \mathbb{R}$, internal energy density $e : Y \times [0, T] \to \mathbb{R}$, internal variables $z : Y \times [0, T] \to Z$ with a sufficiently large vector space Z and the macroscopic absolute temperature $\overline{\theta} \in \mathbb{R}_{>0}$. For a heterogeneous Helmholtz free energy density

$$\psi : Y \times \mathrm{Sym}(d) \times \mathbb{R}_{>0} \times Z \to \mathbb{R}, \quad (x, \varepsilon, \overline{\theta}, z) \mapsto \psi(x, \varepsilon, \overline{\theta}, z),$$

which is related to the internal energy e by

$$e = \psi + s\overline{\theta}, \tag{1}$$

we express stress and entropy by the potential relations

$$\sigma = \frac{\partial \psi}{\partial \varepsilon}(\cdot, \varepsilon, \overline{\theta}, z), \quad \text{and} \quad s = -\frac{\partial \psi}{\partial \overline{\theta}}(\cdot, \varepsilon, \overline{\theta}, z), \tag{2}$$

under the assumption that ψ is differentiable in all arguments except for the first.[39] As a result from the asymptotic homogenization of Chatzigeorgiou et al.,[5] only the macroscopic temperature enters ψ. Thus, the temperature in a microstructure cell corresponding to a macroscopic point can be interpreted as homogeneous.

We assume that the free Helmholtz energy density can be additively decomposed

$$\psi(\cdot, \varepsilon, \overline{\theta}, z) = \psi_{\mathrm{heat}}(\cdot, \overline{\theta}) + \psi_{\mathrm{mech}}(\cdot, \varepsilon, \overline{\theta}, z) \tag{3}$$

into a component ψ_{heat} associated to heat storage and a component ψ_{mech} representing the storage of mechanical energy. This splitting does not reflect physics, but is computationally convenient, cf. Section 3. Many commonly used thermomechanical material models, such as viscoelasticity,[11] elastoplasticity,[5] and viscoplasticity[40] feature a free energy in the form of (3). The heat capacity density at constant strain

$$c_\varepsilon = -\overline{\theta}\frac{\partial^2 \psi}{\partial \overline{\theta}^2}, \tag{4}$$

is typically assumed to be independent of strain ε and internal state z. Under this condition, the temperature dependence of the mechanical free energy ψ_{mech} may at most be linear. Consequently, we also partition the entropy

$$s = s_{\mathrm{heat}}(\cdot, \overline{\theta}) + s_{\mathrm{mech}}(\cdot, \varepsilon, \overline{\theta}, z)$$

with

$$s_{\mathrm{heat}} = -\frac{\partial \psi_{\mathrm{heat}}}{\partial \overline{\theta}} \quad \text{and} \quad s_{\mathrm{mech}} = -\frac{\partial \psi_{\mathrm{mech}}}{\partial \overline{\theta}}.$$

For generalized standard materials, the evolution of internal variables is governed by Biot's equation

$$\frac{\partial \psi}{\partial z}(\cdot, \varepsilon, \overline{\theta}, z) + \frac{\partial \phi}{\partial \dot{z}}(\cdot, \overline{\theta}, \dot{z}) = 0 \tag{5}$$

involving a dissipation potential $\phi : Y \times \mathbb{R}_{>0} \times Z \to \mathbb{R}_{\geq 0}$, $(x, \overline{\theta}, \dot{z}) \mapsto \phi(x, \overline{\theta}, \dot{z})$. We assume that ϕ is convex in its third argument and $\phi(\cdot, \overline{\theta}, 0) = 0$ holds.

For the stress and strain field, the microscopic static balance of linear momentum without volume–force densities

$$\operatorname{div} \sigma = 0, \tag{6}$$

and the kinematic compatibility condition

$$\varepsilon = \overline{\varepsilon} + \nabla^s u \quad \text{with} \quad \overline{\varepsilon} = \langle \varepsilon \rangle_Y \tag{7}$$

hold, where $\langle \cdot \rangle_Y = 1/|Y| \int_Y (\cdot)\, \mathrm{d}V$ denotes the volume average over Y and ∇^s stands for the symmetrized gradient.

The macroscopic temperature is determined by the macroscopic balance of internal energy

$$\overline{\theta}\, \dot{\overline{e}} = -\operatorname{div}_{\overline{x}} \langle q \rangle_Y + \langle \sigma : \dot{\varepsilon} \rangle_Y \quad \text{with} \quad \overline{e} = \langle e \rangle_Y, \tag{8}$$

where we neglect additional source terms and $\operatorname{div}_{\overline{x}}$ denotes the divergence with respect to the position $\overline{x} \in \Omega$ in the macroscopic body $\Omega \subseteq \mathbb{R}^d$. It is common to reformulate the balance of internal energy as a heat equation in terms of the entropy

$$\overline{\theta}\, \dot{\overline{s}} = -\operatorname{div}_{\overline{x}} \langle q \rangle_Y - \left\langle \frac{\partial \psi}{\partial z} \cdot \dot{z} \right\rangle_Y \quad \text{with} \quad \overline{s} = \langle s \rangle_Y, \tag{9}$$

or the temperature

$$c_\varepsilon\, \dot{\overline{\theta}} = -\operatorname{div}_{\overline{x}} \langle q \rangle_Y + \overline{\theta} \left\langle \frac{\partial^2 \psi}{\partial \varepsilon \partial \overline{\theta}} : \dot{\varepsilon} \right\rangle_Y + \overline{\theta} \left\langle \frac{\partial^2 \psi}{\partial z \partial \overline{\theta}} \cdot \dot{z} \right\rangle_Y - \left\langle \frac{\partial \psi}{\partial z} \cdot \dot{z} \right\rangle_Y. \tag{10}$$

Note that, in the small-strain setting, the material time derivative $\dot{(\cdot)}$ reduces to the local time derivative $\frac{\partial (\cdot)}{\partial t}$. As we are only interested in solving the cell problem, that is, we only consider a single macroscopic point, the term $-\operatorname{div}_{\overline{x}} \langle q \rangle_Y$ cannot be further specified and acts as a volumetric heat supply term. Hence, we denote $\mathcal{S} = -\operatorname{div}_{\overline{x}} \langle q \rangle_Y$ and treat $\mathcal{S}$ and $\overline{\varepsilon}$ as boundary conditions. For a treatment in a concurrent multiscale context, cf., for example, Chatzigeorgiou et al.[5] or Tikkarrouchine et al.[11]

3 | SOLUTION SCHEME FOR THE FULLY COUPLED THERMOMECHANICAL CELL PROBLEM

Consider the Hilbert space $V = L^2(Y; \operatorname{Sym}(d))$ of Y-periodic and square integrable stress and strain fields with inner product

$$(S, T) \mapsto \langle S, T \rangle_{L^2} = \langle S : T \rangle_Y, \quad S, T \in V,$$

and the induced norm

$$\|S\|_{L^2} = \sqrt{\langle S, S \rangle_{L^2}}, \quad S \in V.$$

For a certain point in time, we want to find a strain field ε and a macroscopic temperature $\overline{\theta}$ which solve Equations (5)–(8) for prescribed $\overline{\varepsilon}$ and $\mathcal{S}$. For the convenience of the reader, we restrict to pure strain boundary conditions, see Kabel et al.[41] for an extension to mixed boundary conditions. To solve our problem, we consider a fixed time step and apply an implicit Euler discretization in time to our system of equations. We define the operator $M : V \times \mathbb{R}_{>0} \to H_\#^{-1}(Y; \mathbb{R}^d)$, where $H_\#^{-1}(Y; \mathbb{R}^d)$ denotes the space of forces, and the function $H : V \times \mathbb{R}_{>0} \to \mathbb{R}$

$$M(\varepsilon, \overline{\theta}) = \operatorname{div} \frac{\partial \psi}{\partial \varepsilon}(\cdot, \varepsilon, \overline{\theta}, z), \tag{11}$$

$$H(\varepsilon, \overline{\theta}) = \overline{\theta} \langle s_{\text{heat}}(\cdot, \overline{\theta}) + s_{\text{mech}}(\cdot, \varepsilon, \overline{\theta}, z) \rangle_Y - \overline{\theta}\, \overline{s}^n - \Delta t \mathcal{S} + \left\langle \frac{\partial \psi}{\partial z}(\cdot, \varepsilon, \overline{\theta}, z) \cdot (z - z^n) \right\rangle_Y \tag{12}$$

with the mean entropy $\bar{s}^n$ and internal variables z^n at the last converged time step and the time increment Δt. When evaluating $M(\varepsilon, \bar{\theta})$ or $H(\varepsilon, \bar{\theta})$, the internal variables z are computed by solving the discretized Biot's equation

$$\frac{\partial \psi}{\partial z}(\cdot, \varepsilon, \bar{\theta}, z) + \frac{\partial \phi}{\partial \dot{z}}\left(\cdot, \bar{\theta}, \frac{z - z^n}{\Delta t}\right) = 0, \tag{13}$$

for given strain-field ε and temperature $\bar{\theta}$. The thermomechanical cell problem is defined by the system of equations

$$M(\varepsilon, \bar{\theta}) = 0, \tag{14}$$

$$H(\varepsilon, \bar{\theta}) = 0, \tag{15}$$

where (14) describes the mechanical problem for the strain-field ε and (15) is the thermal problem, determining the evolution of the temperature $\bar{\theta}$.

There exist two general approaches for solving the thermomechanically coupled problem. In monolithic schemes, (14) and (15) are solved simultaneously, whereas staggered approaches treat the subproblems (14) and (15) separately.[42,43] Monolithic approaches enjoy unconditional stability, but the resulting system is usually nonsymmetric.[42] Provided each subproblem by itself is symmetric, staggered schemes circumvent this difficulty and thereby enable using more efficient solution algorithms.[44,45] Furthermore, they are convenient in terms of implementation, as existing solvers for the subproblems may be used.[38,46,47] Hence, we focus on staggered algorithms in the following.

Typically, staggered schemes are based on an isothermal split,[42,44] where the mechanical problem is solved for a fixed temperature and the thermal problem is solved for a fixed strain-field. More precisely, for given iterates ε_k and $\bar{\theta}_k$, where $\bar{\theta}_0 = \bar{\theta}^n$ is set to the temperature in the last converged time step, the following steps are performed:

1. Solve $M(\varepsilon, \bar{\theta}_k) = 0$, with fixed temperature $\bar{\theta}_k$ and assign the solution to ε_{k+1}.
2. Solve $H(\varepsilon_{k+1}, \bar{\theta}) = 0$, with fixed strain-field ε_{k+1} and assign the solution to $\bar{\theta}_{k+1}$.

In this context, we distinguish between explicit and implicit staggered schemes. For explicit schemes, steps 1 and 2 are carried out only once, whereas for implicit schemes the steps are repeated until a prescribed convergence criterion is fulfilled.

Thus, explicit schemes are naturally faster. However, they suffer from lower accuracy[47,48] and are prone to instabilities[42,46,49] for problems with strong thermomechanical coupling. To address the latter difficulty, Armero–Simo[42,49] proposed an unconditionally stable adiabatic split, where (14) is solved under the condition $\dot{s} = 0$. In the present work, we do not follow this approach (see below for a discussion) and consider an implicit staggered approach with an isothermal split. Implicit staggered schemes enjoy the same accuracy as monolithic algorithms[43] and have been shown to be more stable than explicit schemes.[46] However, when repeating steps 1 and 2 until convergence, the subproblems (14) and (15) have to be solved multiple times per time step, which is computationally expensive. Therefore, we propose two simplifications to enhance the overall efficiency of the scheme.

First, suppose we have an iterative strain-based fixed point scheme

$$\varepsilon_{k+1} = F(\varepsilon_k, \bar{\theta}), \tag{16}$$

which solves (14) for a fixed temperature $\bar{\theta}$. For better readability, we suppress the possible dependency of f on additional algorithmic parameters and the boundary conditions $\bar{\varepsilon}$. Instead of solving (14) after each temperature update, we only perform a single iteration (16) of the mechanical solver.

The second simplification concerns the temperature update, that is, solving (15). Evaluating $H(\varepsilon, \bar{\theta})$ is computationally expensive, as it involves solving (13) for all points in Y to compute the mechanical entropy $s_{\text{mech}}(\cdot, \varepsilon_k, \bar{\theta}_k, z_k)$ and the dissipation $\frac{\partial \psi}{\partial z}(\cdot, \varepsilon_k, \bar{\theta}_k, z_k) \cdot (z_k - z^n)$, cf. (12). To obtain an efficient algorithm, we wish to avoid this operation outside of (16), that is, without improving our current guess for the strain field. Thus, we propose an additive split of $H(\varepsilon, \bar{\theta})$

$$H(\varepsilon, \bar{\theta}) = H_{\text{impl}}(\bar{\theta}) + H_{\text{expl}}(\varepsilon, \bar{\theta}) \tag{17}$$

into an implicit part $H_{\text{impl}}(\bar{\theta})$

$$H_{\text{impl}}(\bar{\theta}) = \bar{\theta}\langle s_{\text{heat}}(\cdot, \bar{\theta})\rangle_Y - \bar{\theta}\,\bar{s}^n - \Delta t \mathcal{S}$$

and an explicit part $H_{\text{expl}}(\varepsilon, \overline{\theta})$

$$H_{\text{expl}}(\varepsilon, \overline{\theta}) = \overline{\theta}\langle s_{\text{mech}}(\cdot, \varepsilon, \overline{\theta}, z)\rangle_Y + \left\langle \frac{\partial \psi}{\partial z}(\cdot, \varepsilon, \overline{\theta}, z) \cdot (z - z^n) \right\rangle_Y,$$

following our partition of the entropy. We emphasize that this splitting is not physical but computationally convenient. Instead of solving $H(\varepsilon_{k+1}, \overline{\theta}) = 0$ for updating the temperature, we solve $H_{\text{impl}}(\overline{\theta}) + H_{\text{expl}}(\varepsilon_k, \overline{\theta}_k) = 0$. More precisely, we compute the effective mechanical entropy

$$\bar{s}_{\text{mech},k} = \langle s_{\text{mech}}(\cdot, \varepsilon_k, \overline{\theta}_k, z_k)\rangle_Y,$$

as well as the mean dissipation

$$\overline{\mathcal{D}}_k = \left\langle \frac{\partial \psi}{\partial z}(\cdot, \varepsilon_k, \overline{\theta}_k, z_k) \cdot (z_k - z^n) \right\rangle_Y \tag{18}$$

as part of our mechanical iteration (16), cf. Miehe.[50] Subsequently, we solve

$$H_{\text{split}}(\overline{\theta}) = 0 \quad \text{with} \quad H_{\text{split}}(\overline{\theta}) = \overline{\theta}\langle s_{\text{heat}}(\cdot, \overline{\theta})\rangle_Y + \overline{\theta}\,(\bar{s}_{\text{mech},k} - \bar{s}^n) - \Delta t \mathcal{S} + \overline{\mathcal{D}}_k. \tag{19}$$

This is significantly more efficient than solving $H(\varepsilon_{k+1}, \overline{\theta}) = 0$, as it only involves the effective entropy related to heat storage, which is efficiently computed by

$$\langle s_{\text{heat}}(\cdot, \overline{\theta})\rangle_Y = \sum_{j=1}^{N} c_j s_{\text{heat},j}(\overline{\theta}) \tag{20}$$

for an N-phase composite material with volume fractions c_j and phase-specific entropies $s_{\text{heat},j}$.

To summarize, our modified implicit algorithm involves the following steps, which are repeated until the convergence criterion of the mechanical solver is met:

1. Update the strain field $\varepsilon_{k+1} = F(\varepsilon_k, \overline{\theta}_k)$ with a single iteration of the mechanical solver (16). Compute $\bar{s}_{\text{mech},k}$ and $\overline{\mathcal{D}}_k$ as part of the iteration.
2. Solve $H_{\text{split}}(\overline{\theta}) = 0$ and assign the solution to $\overline{\theta}_{k+1}$.

The proposed algorithm is compatible to any mechanical solver in the form of (16), including classical FE-based methods.

For our concrete implementation, we rely on FFT-based solution schemes, due to their computational efficiency.[15-17] In particular, we consider Moulinec–Suquet's basic scheme,[14] the Barzilai–Borwein method,[25] and the inexact Newton–CG method,[23] cf. Appendix A. Typically, the iteration scheme (16) involves applying the operator $\Gamma = \nabla^s(\text{div}\,\nabla^s)^{-1}\text{div}$ in Fourier space and evaluating material law $\sigma = \frac{\partial \psi}{\partial \varepsilon}(\cdot, \overline{\theta}, \varepsilon, z)$. As convergence criterion for the static equilibrium (14), we use

$$\frac{\|\Gamma : \sigma\|_{L^2}}{\|\langle \sigma \rangle Y\|_{L^2}} \leq \delta_{\text{mech}}, \tag{21}$$

see section 5 of Schneider et al.[51] for further details. The mean mechanical entropy $\bar{s}_{\text{mech},k}$ and the mean dissipation $\overline{\mathcal{D}}_k$ are computed when evaluating the material law. For the temperature update we use Newton's method, that is, we iterate

$$\overline{\theta}^{i+1} = \overline{\theta}^{i} - \frac{H_{\text{split}}(\overline{\theta}^{i})}{H'_{\text{split}}(\overline{\theta}^{i})} \quad \text{with } \overline{\theta}^{0} = \overline{\theta}_k,$$

and

$$H'_{\text{split}}(\overline{\theta}) = \overline{\theta}\langle s'_{\text{heat}}(\cdot, \overline{\theta})\rangle_Y + \langle s_{\text{heat}}(\cdot, \overline{\theta})\rangle_Y + \bar{s}_{\text{mech},k} - \bar{s}^n,$$

until the criterion

$$\left| \frac{H_{\text{split}}(\overline{\theta})}{\overline{\theta}\langle s_{\text{heat}}(\cdot,\overline{\theta})\rangle_Y + \overline{\theta}\,\overline{s}_{\text{mech},k}} \right| < \delta_{\text{heat}} \tag{22}$$

is met. Thus, we set $\overline{\theta}_{k+1} = \overline{\theta}^i$. If the convergence criterion (21) is met, we proceed to the next time step. Otherwise, we repeat updates (16) and (19). The algorithm is summarized in Algorithm 1.

Algorithm 1. Implicit staggered solution scheme ($\overline{\varepsilon}$, $\text{maxit}_{\text{mech}}$, δ_{mech}, $\mathcal{S}$, $\text{maxit}_{\text{heat}}$, δ_{heat})

Set initial values for $\bar{\theta}$ and ε
$k \leftarrow 0$
$r_{\text{mech}} \leftarrow 1$
while $k < \text{maxit}_{\text{mech}}$ **and** $r_{\text{mech}} > \delta_{\text{mech}}$ **do**
  $k \leftarrow k + 1$
  $\begin{bmatrix} \varepsilon \\ \bar{s}_{\text{mech}} \\ \overline{D} \\ r_{\text{mech}} \end{bmatrix} \leftarrow \begin{bmatrix} F(\varepsilon,\bar{\theta}) \\ \left\langle s_{\text{mech}}(\cdot,\varepsilon,\bar{\theta},z)\right\rangle_Y \\ \left\langle \frac{\partial\psi}{\partial z}(\cdot,\varepsilon,\bar{\theta},z)\cdot(z-z^n)\right\rangle_Y \\ \|\Gamma : \sigma\|_{L^2}/\|\langle\sigma\rangle_Y\|_{L^2} \end{bmatrix}$ ▷ Isothermal step of mechanical solver (16)
  $r_{\text{heat}} \leftarrow 1$
  $i \leftarrow 0$
  while $i < \text{maxit}_{\text{heat}}$ **and** $r_{\text{heat}} > \delta_{\text{heat}}$ **do** ▷ Temperature update (19)
    $i \leftarrow i + 1$
    $H \leftarrow \bar{\theta}\left\langle s_{\text{heat}}(\cdot,\bar{\theta})\right\rangle_Y + \bar{\theta}\,(\bar{s}_{\text{mech}} - \bar{s}^n) - \Delta t\mathcal{S} + \overline{D}$
    $H' \leftarrow \bar{\theta}\left\langle s'_{\text{heat}}(\cdot,\bar{\theta})\right\rangle_Y + \left\langle s_{\text{heat}}(\cdot,\bar{\theta})\right\rangle_Y + \bar{s}_{\text{mech}} - \bar{s}^n$
    $r_{\text{heat}} \leftarrow |H/(\bar{\theta}\left\langle s_{\text{heat}}(\cdot,\bar{\theta})\right\rangle_Y + \bar{\theta}\,\bar{s}_{\text{mech}})|$
    $\bar{\theta} \leftarrow \bar{\theta} - H/H'$
  end while
end while
return $\bar{\theta}$, ε

Several remarks are in order:

1. For the temperature update, we use the entropy-based heat equation (9) instead of the more common temperature-based formulation (10). Consider the change in s_{mech} under the assumption that the heat capacity c_ε, as defined in (4), depends only on the temperature. Using the implicit Euler time discretization on $\overline{\theta}\dot{s}_{\text{heat}}$ in (9) yields

$$\overline{\theta}\frac{s_{\text{heat}}(\overline{\theta}) - s^n_{\text{heat}}}{\Delta t}.$$

   If, alternatively, we discretized the corresponding term $c_\varepsilon(\overline{\theta})\dot{\overline{\theta}}$ in (10), we obtain

$$\overline{\theta}\frac{\partial s_{\text{heat}}}{\partial\overline{\theta}}(\overline{\theta})\frac{\overline{\theta} - \overline{\theta}^n}{\Delta t}.$$

   Apparently, the change in entropy is basically linearized. Hence, to obtain higher precision for large time increments we prefer using (9).
2. For the temperature update (19), we only consider the temperature dependency of the entropy related to heat storage $\bar{s}_{\text{heat}}$, whereas $\bar{s}_{\text{mech}}$ and $\overline{D}$ remain fixed. Indeed, if the heat capacity c_ε depends only on the temperature, $\bar{s}_{\text{mech}}$ is temperature independent and $\overline{D}$ is at most a linear function of the temperature. Thus, as the strain field

ε converges, changes in subsequent iterates $\overline{\theta}_k$ become small. As a result, the solution of (19) approaches the solution of (15).

3. Due to the homogeneity of the macroscopic temperature $\overline{\theta}$, computing the mean entropy (20) is comparatively inexpensive. Thus, solving the scalar equation (19) introduces no significant computational overhead. Compared with solving the isothermal mechanical problem, higher computation times may still arise for the thermomechanically coupled case, due to two factors. First, the iterative solver (16) may require more iterations to converge, depending on the thermomechanical coupling of the composite, that is, the temperature dependence of the material laws and the magnitude of $\bar{s}_{\text{mech}}$ and $\overline{\mathcal{D}}$. Second, evaluating $\bar{s}_{\text{mech}}$ and $\overline{\mathcal{D}}$ may affect the overall runtime of the algorithm, provided the associated computational effort is similar to the evaluation of the material law and the Γ operator.
4. Armero–Simo[42,49] analyzed different operator splits for thermomechanically coupled problems and found that the explicit isothermal split, that is, an isothermal mechanical step followed by a temperature update, is only conditionally stable. As an alternative, they proposed the unconditionally stable adiabatic split, where the mechanical problem is solved under the condition $\dot{s} = 0$. For the present algorithm, we rely on the isothermal split as it is more convenient from the viewpoint of implementation. Suppose we already have an existing code for a purely mechanics-based solution scheme. For the isothermal split, only an update of the temperature dependent material parameters and the computation of s_{mech} and $\mathcal{D}$ have to be added to the already implemented material law. For the adiabatic split, on the other hand, simple reduced forms of the material law, which identically fulfill $\dot{s} = 0$, can only be derived in special cases such as linear thermoelasticity.[42] For more complex material laws with arbitrary temperature dependencies, the implementation of an additional adiabatic formulation may be cumbersome or even require an iterative local solution scheme. Thus, for tackling the issue of instability, we prefer using an implicit staggered approach based on an isothermal split.[46] Indeed, we encountered no numerical instabilities in our numerical experiments in Section 4, even for a composite with strong thermomechanical coupling.

4 | NUMERICAL DEMONSTRATIONS

4.1 | Setup

Algorithm 1 for thermomechanically coupled problems was implemented in an in-house FFT-based computational homogenization code written in Python 3.7 with FFTW[18] bindings. Applying Γ and evaluating the material law were integrated as Cython extensions[52] and parallelized using OpenMP. Throughout, we rely on the discretization by trigonometric polynomials introduced by Moulinec–Suquet.[14] As convergence criterion for the iterative FFT-based solver, we use (21)

$$\frac{\|\Gamma : \sigma\|_{L^2}}{\|\langle\sigma\rangle_Y\|_{L^2}} \leq \delta_{\text{mech}}$$

with a prescribed tolerance of $\delta_{\text{mech}} = 10^{-5}$. The tolerance for the convergence criterion (22) of the temperature update

$$\left| \frac{H_{\text{split}}(\overline{\theta})}{\overline{\theta}\langle s_{\text{heat}}(\cdot, \overline{\theta})\rangle_Y + \overline{\theta}\ \bar{s}_{\text{mech},k}} \right| < \delta_{\text{heat}}$$

is set to $\delta_{\text{heat}} = 10^{-4}$.

For the computations on the two-dimensional microstructure in Section 4.2, a desktop computer with 32 GB RAM and a six-core Intel i7-8700K CPU was used. The computations on the three-dimensional microstructure in Section 4.3 were performed on a workstation with 512 GB RAM and two 12-core Intel Xeon(R) Gold 6146.

4.2 | Continuous glass–fiber reinforced polypropylene

In the following example, we consider a composite consisting of a polypropylene matrix unidirectionally reinforced by continuous glass fibers with a volume fraction of 30%. The microstructure, cf. Figure 1, is modeled as a two-dimensional periodic cell with a resolution of 512^2, containing 200 fibers. It was generated using the adaptive shrinking cell algorithm of Torquato–Jiao.[53]

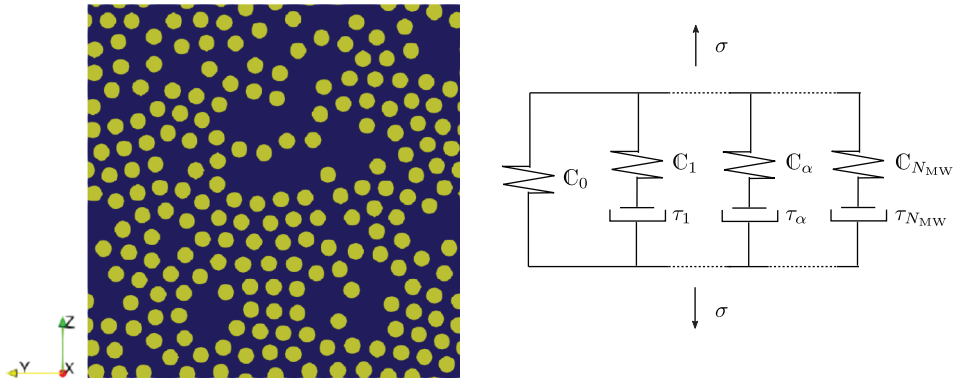

FIGURE 1 Continuous glass–fiber reinforced polypropylene: microstructure and schematic of the generalized Maxwell model for polypropylene

TABLE 1 Material parameters of the glass fibers[11]

Thermal expansion	$\alpha_0 = 9 \times 10^{-6}$ 1/K
Heat capacity	$c_0 = 2.1 \times 10^6$ J/(m^3 K)
Shear modulus	$G = 28.6$ GPa

The glass fibers are modeled as an isotropic linear thermoelastic material. The free energy related to heat storage reads

$$\psi_{\mathrm{heat}}(\theta) = c_0 \left[(\theta - \theta_{\mathrm{ref}}) - \theta \ln \left(\frac{\theta}{\theta_{\mathrm{ref}}} \right) \right],$$

and corresponds to a material with a constant heat capacity $c_\varepsilon(\theta) = c_0$. Typically, for solids, states of constant strain are hard to realize under fluctuating temperatures. Hence, the heat capacity c_ε at constant strain is usually not measured experimentally. However, its value is typically close to the heat capacity c_σ at constant stress. The mechanical part of the free energy is given by

$$\psi_{\mathrm{mech}}(\varepsilon, \theta) = \frac{1}{2} \varepsilon : \mathbb{C} : \varepsilon - \varepsilon : \mathbb{C} : (\alpha(\theta - \theta_{\mathrm{ref}})),$$

implying the stress–strain relation

$$\sigma = \mathbb{C} : (\varepsilon - \alpha(\theta - \theta_{\mathrm{ref}}))$$

with a stiffness tensor $\mathbb{C}$ and a thermal expansion tensor $\alpha \in \mathrm{Sym}(d)$. The associated entropies read

$$s_{\mathrm{heat}}(\theta) = c_0 \ln \left(\frac{\theta}{\theta_{\mathrm{ref}}} \right) \quad \text{and} \quad s_{\mathrm{mech}}(\varepsilon) = \varepsilon : \mathbb{C} : \alpha.$$

As the material is elastic, no energy is dissipated, that is, $\mathcal{D} = 0$, and the thermomechanical coupling is governed solely by s_{mech}. Changes in s_{mech} cause self-heating under hydrostatic compression and self-cooling under hydrostatic extension. This phenomenon is commonly referred to as thermoelastic coupling effect, cf. section 13.2 in Haupt,[54] or Gough–Joule effect, cf. section 96 in Truesdell–Noll.[55] For the glass fibers, we assume that both stiffness and thermal expansion are isotropic, that is,

$$\mathbb{C} = 3K\mathbb{P}_1 + 2G\mathbb{P}_2 \quad \text{and} \quad \alpha = \alpha_0 \mathrm{Id}$$

with bulk modulus K, shear modulus G, and isotropic coefficient of thermal expansion α_0. By $\mathbb{P}_1$ and $\mathbb{P}_2$ we denote the projectors onto the spherical and deviatoric $d \times d$ matrices, respectively. The parameters of the model are taken from Tikkarrouchine et al.[11] and listed in Table 1.

For the polypropylene matrix, we assume a linear thermoviscoelastic model based on a generalized Maxwell model, cf. Figure 1 and section 3.5.1 in Tschoegl's book.[56] For models accounting for effects outside of the viscoelastic domain, we refer, for example, to Krairi et al.[57] and Benaarbia et al.[58] for extensions to viscoplasticity and damage, and Tscharnauter et al.[59] for a study on polypropylene. Based on the caloric data in table 18.10 in the *Springer Handbook of Materials Data*,[60] we assume a heat-storage related free energy of the form

$$\psi_{\text{heat}}(\theta) = c_0 \left[(1 - k\theta_{\text{ref}}) \left((\theta - \theta_{\text{ref}}) - \theta \ln \left(\frac{\theta}{\theta_{\text{ref}}} \right) \right) - \frac{k}{2} (\theta - \theta_{\text{ref}})^2 \right],$$

corresponding to a linear heat capacity

$$c_\varepsilon(\theta) = c_0[1 + k(\theta - \theta_{\text{ref}})].$$

The energy stored the generalized Maxwell model with N_{MW} Maxwell elements reads

$$\begin{aligned} \psi_{\text{mech}}(\varepsilon, \theta, \varepsilon_{\text{v}\alpha}) = \frac{1}{2} \varepsilon : \mathbb{C}_0 : \varepsilon + \sum_{\alpha=1}^{N_{\text{MW}}} \frac{1}{2} (\varepsilon - \varepsilon_{\text{v}\alpha}) : \mathbb{C}_\alpha : (\varepsilon - \varepsilon_{\text{v}\alpha}) \\ - \varepsilon : \mathbb{C}_0 : (\alpha(\theta - \theta_{\text{ref}})) - \sum_{\alpha=1}^{N_{\text{MW}}} (\varepsilon - \varepsilon_{\text{v}\alpha}) : \mathbb{C}_\alpha : (\alpha(\theta - \theta_{\text{ref}})). \end{aligned}$$

Consequently, the stress computes as

$$\sigma = \mathbb{C}_0 : (\varepsilon - \alpha(\theta - \theta_{\text{ref}})) + \sum_{\alpha=1}^{N_{\text{MW}}} \mathbb{C}_\alpha : (\varepsilon - \varepsilon_{\text{v}\alpha} - \alpha(\theta - \theta_{\text{ref}})).$$

We assume that the viscosity tensor associated to a dashpot of the generalized Maxwell model has the form

$$\mathbb{V}_\alpha = a(\theta) \tau_\alpha \mathbb{C}_\alpha,$$

where $a : \mathbb{R}_{>0} \to \mathbb{R}$ denotes a temperature-dependent shift function. The corresponding fluidity $\mathbb{F}_\alpha$ is defined by the pseudoinverse

$$\mathbb{F}_\alpha = (\mathbb{V}_\alpha)^\dagger = \frac{1}{a(\theta)\tau_\alpha} (\mathbb{C}_\alpha)^\dagger.$$

In terms of the partial stresses

$$\sigma_{\text{v}\alpha} = \mathbb{C}_\alpha : (\varepsilon - \varepsilon_{\text{v}\alpha} - \alpha(\theta - \theta_{\text{ref}})),$$

the evolution equation for the viscous strains reads

$$\dot{\varepsilon}_{\text{v}\alpha} = \mathbb{F}_\alpha : \sigma_{\text{v}\alpha}.$$

For simplicity, we assume that polypropylene is isotropic and linear elastic in dilation, cf. section 9.4 in Brinson–Brinson.[61] More precisely, the stiffness tensors and the thermal expansion tensor have the form

$$\mathbb{C}_0 = 3K_0 \mathbb{P}_1 + 2G_0 \mathbb{P}_2, \quad \mathbb{C}_\alpha = 2G_\alpha \mathbb{P}_2, \quad \text{and} \quad \alpha = \alpha_0 \text{Id}.$$

In this particular case, the viscous strains $\varepsilon_{\text{v}\alpha}$ are purely deviatoric and independent of thermal expansion. The shift function a describes the time-temperature dependency of the material. At room temperature $\theta_{\text{ref}} = 293.15$ K, polypropylene is above its glass transition temperature $\theta_{\text{glass}} \approx 273.15$ K. Hence, we use the Williams–Landel–Ferry (WLF) equation[62] as ansatz for the shift function

TABLE 2 Material parameters of polypropylene

Thermal expansion[60]	$\alpha_0 = 1.91 \times 10^{-4}$ 1/K
Heat capacity[60]	$c_0 = 1.512 \times 10^6$ J/(m^3 K)
	$k = 4.6 \times 10^{-3}$
WLF constants[65]	$C_1 = 45$
	$C_2 = 158$ K
Bulk modulus[65]	$K_0 = 4930$ MPa
Shear modulus[65]	$G_0 = 415.6$ MPa
Maxwell elements[65]	$\tau_1 = 10^{-4}$ s $G_1 = 154.8$ MPa $\tau_6 = 10$ s $G_6 = 38.4$ MPa
	$\tau_2 = 10^{-3}$ s $G_2 = 127.0$ MPa $\tau_7 = 10^2$ s $G_7 = 36.7$ MPa
	$\tau_3 = 10^{-2}$ s $G_3 = 97.6$ MPa $\tau_8 = 10^3$ s $G_8 = 31.5$ MPa
	$\tau_4 = 10^{-1}$ s $G_4 = 72.3$ MPa $\tau_9 = 10^4$ s $G_9 = 30.6$ MPa
	$\tau_5 = 1$ s $G_5 = 50.9$ MPa

$$\log_{10} a(\theta) = -\frac{C_1(\theta - \theta_{\text{ref}})}{C_2 + \theta - \theta_{\text{ref}}}. \tag{23}$$

For the present study, we restrict to linear viscoelastic behavior and focus on the effects induced by the thermomechanical coupling. In particular, we omit a possible pressure dependence of the shift factor as suggested by Fillers–Tschoegl[63] based on free-volume considerations.

For our implementation, we use the time-integration scheme of Taylor et al.,[64] which is based on the partial stresses $\sigma_{\text{v}\alpha}$ instead of the viscous strains $\varepsilon_{\text{v}\alpha}$. The update reads

$$\sigma_{\text{v}\alpha} = \exp\left(-\frac{\Delta\xi}{\tau_\alpha}\right)\sigma^n_{\text{v}\alpha} + \frac{\left(1 - \exp\left(-\frac{\Delta\xi}{\tau_\alpha}\right)\right)}{\frac{\Delta\xi}{\tau_\alpha}}\mathbb{C}_\alpha : (\varepsilon - \varepsilon^n + \alpha(\theta - \theta^n)),$$

where $(\cdot)^n$ denotes the value of the last converged time step and ξ is a reduced time defined via

$$\xi = \int_0^t \frac{1}{\alpha(\theta(\tau))} d\tau.$$

We compute the change in reduced time $\Delta\xi = \xi - \xi^n$ by a five-point Gauss quadrature, assuming a constant temperature rate. The entropies and dissipation in terms of the partial stresses $\sigma_{\text{v}\alpha}$ read

$$s_{\text{heat}}(\theta) = c_0\left[(1 - k\theta_{\text{ref}})\ln\left(\frac{\theta}{\theta_{\text{ref}}}\right) + k(\theta - \theta_{\text{ref}})\right],$$

$$s_{\text{mech}}(\varepsilon, \theta, \sigma_{\text{v}\alpha}) = \varepsilon : \mathbb{C}_0 : \alpha + \sum_{\alpha=1}^{N_{\text{MW}}} \alpha : [\sigma_{\text{v}\alpha} + \mathbb{C}_\alpha : (\alpha(\theta - \theta_{\text{ref}}))],$$

$$\mathcal{D} = \sum_{\alpha=1}^{N_{\text{MW}}} \sigma_{\text{v}\alpha} : \mathbb{F}_\alpha : \sigma_{\text{v}\alpha}.$$

The used material parameters are listed in Table 2. The caloric parameters were chosen based on tables 18.9 and 18.10 in the *Springer Handbook of Materials Data*[60] and the viscoelastic parameters are taken from the experimental study by Kehrer et al.[65] Note that Kehrer et al.[65] characterized the behavior of polypropylene over a wide range of frequencies and temperatures, using 27 Maxwell elements for their model. For the present study, we restrict to moderate temperature and frequency changes and only consider nine elements with time constants $\tau_\alpha \in [10^{-4}, 10^4]$ in order to reduce computation times. The shear moduli of the elements with $\tau_\alpha > 10^4$ are added to the elastic shear modulus G_0, whereas the elements with $\tau_\alpha < 10^{-4}$ were omitted.

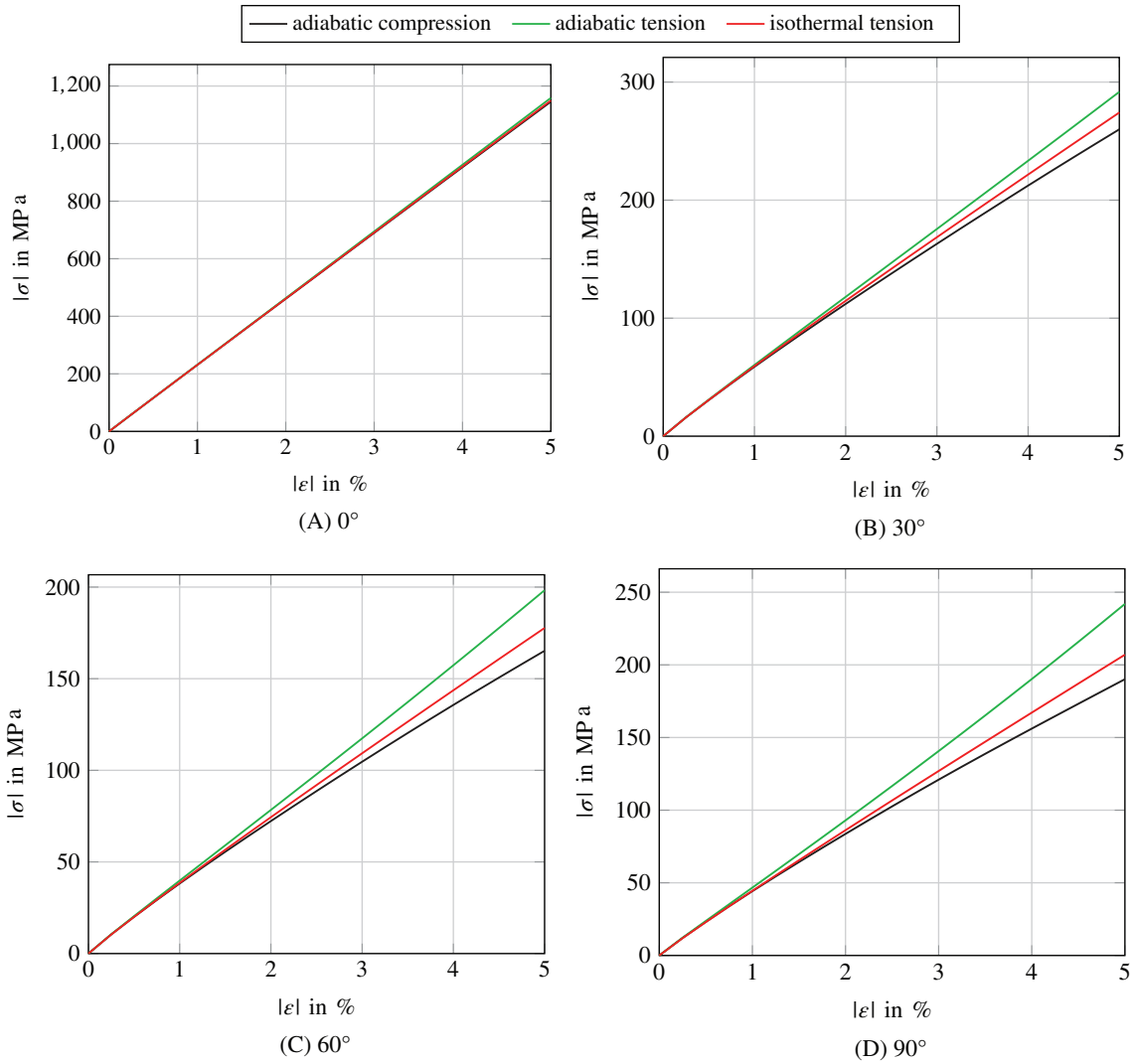

FIGURE 2 Continuous glass–fiber reinforced polypropylene: stress vs strain at various loading angles in the xz-plane with respect to the x-direction

4.2.1 | Uniaxial extension

In our first set of experiments, we take a look at the stress-strain behavior under uniaxial extension and compression. We want to assess the strength of the thermomechanical coupling for the investigated composite microstructure. In addition, we are interested in the performance of the different FFT-based solution algorithms in Appendix A in conjunction with the staggered thermomechanical solution scheme in Algorithm 1. To this end, we apply mixed boundary conditions, cf. Kabel et al.,[41] corresponding to strain-controlled uniaxial extension/compression to 5% with a strain rate of 1/s at various loading angles in the xz-plane with respect to the x-direction, that is, the fiber direction. For the first set of computations, we consider adiabatic conditions, that is, $\mathcal{S} = 0$, where self-heating/-cooling of the material is expected. The second set of computations is performed with a fixed temperature of $\theta_{\text{ref}} = 293.15\ K$ as reference.

The resulting stress–strain curves are plotted in Figure 2. In the isothermal setting, there is no distinction between tension and compression and we observe a linear relation between stresses and strains. For the loading under adiabatic conditions, however, the thermomechanical coupling induces an effectively nonlinear behavior. To be more precise, under compression, s_{mech} decreases, which leads to a rise in temperature, resulting in the softening of the polypropylene matrix. Conversely, under tension s_{mech} increases, leading to a lower temperature and the stiffening of polypropylene. Two factors contribute to the strength of the observed thermomechanical coupling. First, due to its high thermal expansion coefficient α, the Gough–Joule effect, that is, the strain-induced change of s_{mech} is rather pronounced for polypropylene. Second,

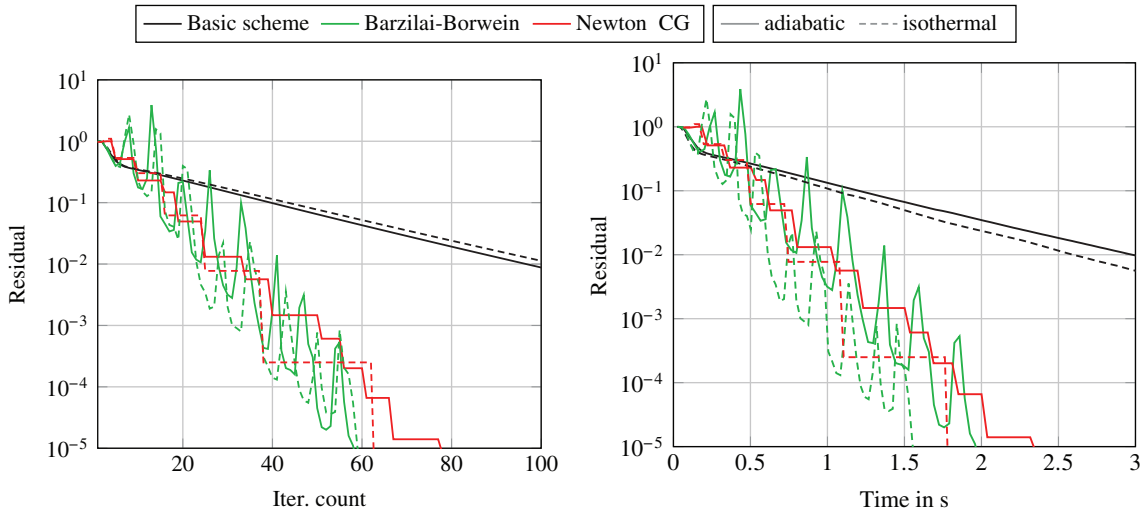

(A) Residual vs iteration count

(B) Residual vs computation time

FIGURE 3 Continuous glass–fiber reinforced polypropylene: performance comparison for 5% uniaxial extension in z-direction in a single load step

the mechanical behavior of polypropylene is very sensitive to temperature changes in the vicinity of its glass transition temperature, as encapsulated by the WLF equation (23). Note that the computations for the 0° load angle represent an exception to these observations. In this case, the fibers carry most of the load and we observe no difference between isothermal and adiabatic computations, due to temperature independence of their stiffness.

4.2.2 | Performance comparison for a single load step

Next, we take a closer look at the performance of the different FFT-based solution schemes. In particular, we are interested how their convergence behavior changes in case of strong thermomechanical coupling, compared with the isothermal setting. Hence, we consider the load case of uniaxial extension at a 90° load angle, where the coupling is most pronounced. First, the performance is evaluated for a single load step up to 5% strain.

The residual is plotted as a function of iteration counts and computation time in Figure 3. Note that the convergence behavior of the Newton–CG method in the adiabatic setting is distinctly different in comparison with the isothermal computation. For the isothermal case, the decrease of the residual gradually grows in subsequent Newton iterations. Due to the adaptive forcing-term choice of Eisenstat–Walker,[66] the linear system is thus solved to higher accuracy. In contrast, the convergence rate with respect to Newton iterations is roughly constant for the adiabatic computation. This is due to the fact that we do not consider the temperature dependence of the material behavior in the computation of the Hessian. Thus, the linear approximation of the gradient is less precise than for the isothermal computation. With respect to the overall performance, this effect is somewhat alleviated by Eisenstat–Walker's forcing-term choice,[66] as the linear system is solved to lower accuracy, thereby reducing the cost of each Newton iteration. Even though, Newton–CG requires 75% more Newton iterations in the adiabatic setting, the runtime only increases by about 30%, cf. Table 3.

For the basic scheme, the convergence rate in the adiabatic and isothermal setting is nearly identical. The same is true for the Barzilai–Borwein method, which displays its characteristic nonmonotone behavior and converges in much fewer iterations than the basic scheme, cf. Table 3. Even though the iteration counts of both schemes are roughly identical for both settings, the overall computation times are slightly higher for the adiabatic computations.

A look at the computational cost of the most expensive operations, that is, the material law, the FFTs and the Γ-operator, clarifies this phenomenon. In Table 4, the average computation times per application of these operations are listed for the 0° load case solved by the Barzilai–Borwein scheme. Notably, for the adiabatic setting, the additional computation of $\mathcal{D}$ and s_{mech} in the material law increases its time per application by about 70%. Thus, the overall cost per iteration ends up 30% higher. The same is true for the basic scheme.

		Isothermal	Adiabatic
Basic scheme	Iter. count	349	323
	Comp. time (s)	9.34	10.04
Barzilai–Borwein	Iter. count	60	59
	Comp. time (s)	1.60	2.01
Newton–CG	Newton iter. count	8	14
	CG iter. count	55	64
	Comp. time (s)	1.80	2.38

TABLE 3 Continuous glass–fiber reinforced polypropylene: iteration counts and computation times for 5% uniaxial extension in z-direction in a single load step

Mean comp. time per application (ms)	Isothermal	Adiabatic
Material law	9.6	16.2
FFT	9.7	9.6
Γ^0 operator	2.4	2.5

TABLE 4 Continuous glass–fiber reinforced polypropylene: computation time per application of the most expensive operations for loading in z-direction and solved by the Barzilai–Borwein method in a single load step

Comparing the overall performance of the schemes, we observe that the Barzilai–Borwein method is the fastest for both the isothermal and adiabatic setting. The Newton–CG method is only slightly slower but suffers from increased iteration counts for the adiabatic case. The basic scheme is by far the slowest, taking five to six times longer than the Barzilai–Borwein method.

4.2.3 | Performance comparison for 20 load steps

Next, we investigate the performance of the solvers, when subdividing the strain loading of 5% into 20 equally spaced load steps. An affine-linear extrapolation[14] is applied at the beginning of each load step to obtain an initial guess for the strain field. The total iteration counts and computation times of the different solvers in each load step are plotted in Figure 4.

For all solvers, the iteration counts decrease up to step 5 as the affine-linear extrapolation takes effect. For the isothermal computations, the iteration counts further decrease after this point, due to the linear stress–strain behavior. In contrast, the iteration counts stagnate or, in case of the basic scheme, even increase for the adiabatic computations. This coincides with the onset of the effectively nonlinear material behavior for uniaxial strains larger than 1%, cf. Figure 2(D). Hence, the affine-linear extrapolation becomes less effective, which leads to higher iteration counts compared with the isothermal computations. Note that for a material which already behaves nonlinearly under isothermal conditions, this difference between adiabatic and isothermal computations is expected to be less pronounced (Table 5).

As for the loading in a single step, the Barzilai–Borwein method is fastest. Its computation time for the adiabatic case increases by roughly 35%, due to higher iteration counts and the additional cost per iteration. The performance of the Newton–CG method is nearly identical to the Barzilai–Borwein method for the isothermal computation. However, it exhibits a larger decrease in performance for the adiabatic computation, with an increase in computation time by nearly 60%. For the basic scheme, the iteration counts are roughly identical for the isothermal and the adiabatic setting. In the first nine steps, the adiabatic computation converges faster, as a consequence of the stiffening due to self-cooling and the resulting reduction in material contrast. For the subsequent steps, the isothermal computation requires fewer iterations, due to the more effective affine-linear extrapolation. Fortuitously, these effects roughly cancel each other out. Overall, the basic scheme is still the slowest, taking three to four times longer than the Barzilai–Borwein method to converge.

To summarize, we observe that the convergence behavior of the basic scheme and the Barzilai–Borwein method in conjunction with Algorithm 1 is similar to their convergence behavior under isothermal conditions, even for a composite with strong thermomechanical coupling. The computation times for the thermomechanically coupled computations increase by roughly 30% for both schemes, which is mainly due to the additional cost of computing the dissipation D and mechanical entropy s_{mech} in the material law. The Newton–CG method suffered the highest decrease

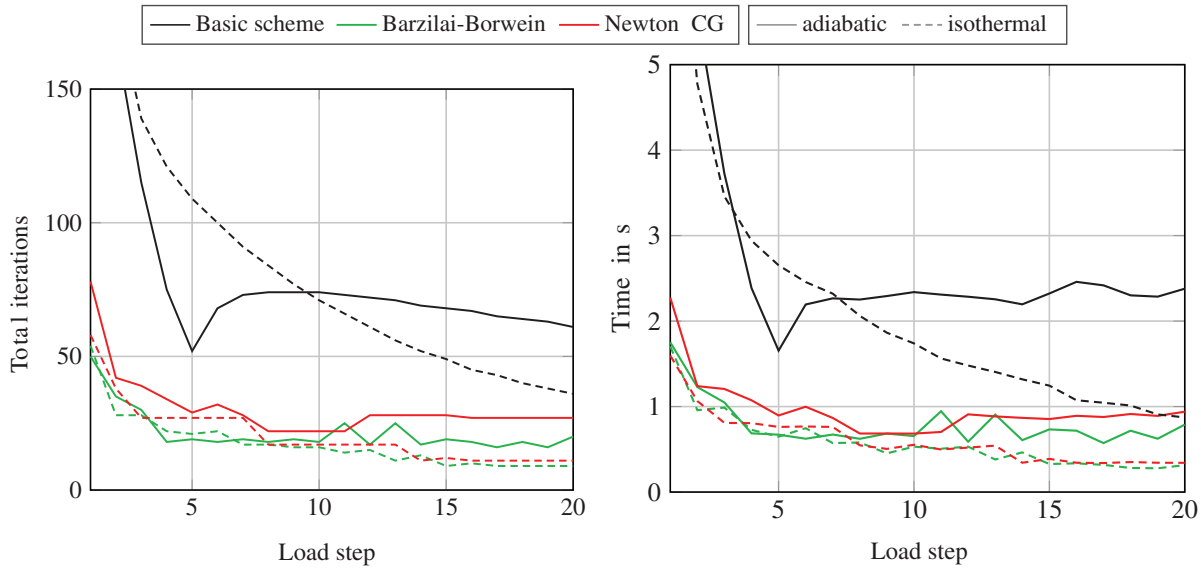

(A) Iteration count vs load step (B) Computation time vs load step

FIGURE 4 Continuous glass–fiber reinforced polypropylene: performance comparison for 5% uniaxial extension in z-direction in 20 load steps

TABLE 5 Continuous glass–fiber reinforced polypropylene: mean iteration counts and computation times for 5% uniaxial extension in z-direction and 20 load steps

		Isothermal	Adiabatic
Basic scheme	Mean iter. count	87.80	87.05
	Mean comp. time (s)	2.23	2.87
Barzilai–Borwein	Mean iter. count	17.45	22.00
	Mean comp. time (s)	0.58	0.79
Newton–CG	Mean Newton iter. count	5.15	7.70
	Mean CG iter. count	15.40	23.15
	Mean Comp. time (s)	0.61	0.97

in performance for the coupled computations, as the temperature dependence is neglected in the Hessian computation. This leads to a significant increase in Newton- and CG-iterations, in addition to the higher cost per Newton iteration.

Considering the overall performance, the Barzilai–Borwein method and the Newton–CG method are the fastest solvers. Due to its lower memory requirements and its more robust convergence behavior in the thermomechanically coupled computations, we use the Barzilai–Borwein method for all following computations.

4.3 | Planar short glass–fiber reinforced polypropylene

Motivated by the numerical experiments in the last section, we investigate a more complex microstructure, cf. Figure 5. We consider a polypropylene matrix reinforced by 1130 short glass–fibers with an aspect ratio of 20. The fiber volume fraction amounts to 13.2%, corresponding to mass fraction of 30%. The microstructure was generated by the sequential addition and migration algorithm[67] and discretized by $512 \times 512 \times 64$ voxels. The second-order fiber-orientation tensor reads $A = \mathrm{diag}(0.45, 0.45, 0.1)$, cf. Advani–Tucker.[68] For the following investigations, we use the same material models and parameters as in Section 4.2.

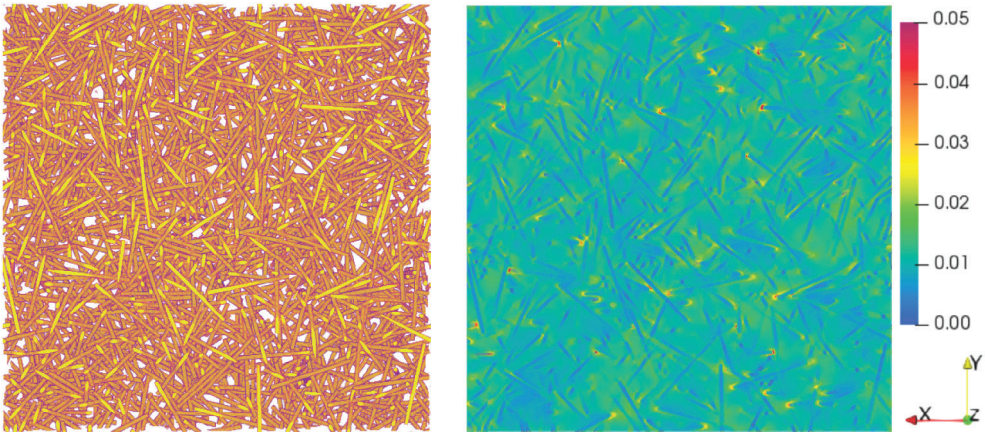

(A) Microstructure (B) Von Mises equivalent strain

FIGURE 5 Short glass–fiber reinforced polypropylene: microstructure and von Mises equivalent strain after 1% uniaxial extension in x-direction

4.3.1 | Dynamic mechanical analysis

The macroscopic behavior of viscoelastic composites is often investigated under steady-state oscillations with a fixed frequency $f \in \mathbb{R}_{\geq 0}$, cf. section 5.5 in Brinson–Brinson.[61] This is commonly called dynamic–mechanical analysis (DMA). Suppose a linear viscoelastic material is harmonically excited by uniaxial tension/compression where the strain component in loading direction is given by

$$\varepsilon(t) = \varepsilon_{\text{amp}} \sin(\omega t), \tag{24}$$

with the strain amplitude $\varepsilon_{\text{amp}} \in \mathbb{R}_{\geq 0}$ and the angular frequency $\omega = 2\pi f$. The stress response of the material in loading direction reads

$$\sigma(t) = \sigma_{\text{amp}} \sin(\omega t + \delta) \tag{25}$$

with the stress amplitude $\sigma_{\text{amp}} \in \mathbb{R}_{\geq 0}$ and phase difference $\delta \in [0, \pi/2]$. Typical characteristics for the material are the storage modulus

$$E' = \frac{\sigma_{\text{amp}}}{\varepsilon_{\text{amp}}} \cos(\delta) \tag{26}$$

and loss modulus

$$E'' = \frac{\sigma_{\text{amp}}}{\varepsilon_{\text{amp}}} \sin(\delta). \tag{27}$$

The storage modulus is related to the average elastic energy stored in a load cycle

$$\psi_{\text{cycle}} = \frac{1}{4} \varepsilon_{\text{amp}}^2 E'$$

and serves as a measure of the material's elastic stiffness. The loss modulus is proportional to the energy dissipated over a load cycle

$$\mathcal{D}_{\text{cycle}} = \pi \varepsilon_{\text{amp}}^2 E'', \tag{28}$$

cf. section 9.1 in Tschoegl.[56] Thus, E'' is of particular interest in cases of harmonic loadings with high cycle counts. For instance in fatigue experiments,[69,70] the dissipated energy accumulates, leading to an increase of temperature over time.

For linear viscoelastic material models, such as the generalized Maxwell model for polypropylene, E' and E'' can be computed analytically in the isothermal setting, cf. section 11.1 in Tschoegl.[56] However, as we have seen in Section 4.2.1,

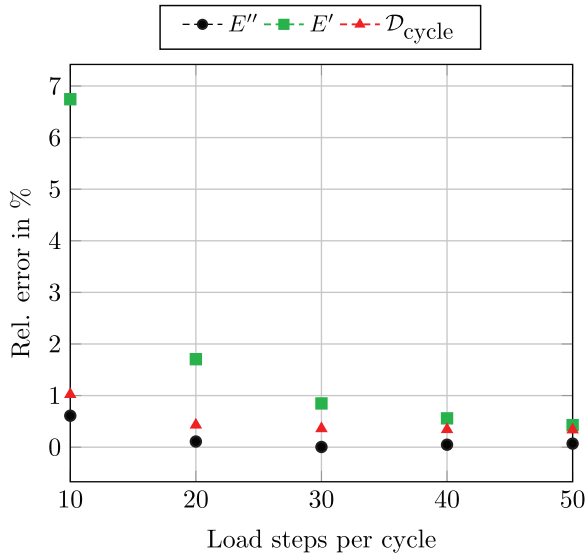

FIGURE 6 Polypropylene: relative error between analytic values and the results of the virtual DMA tests for E', E'', and $\mathcal{D}_{\text{cycle}}$ as a function of load steps per cycle

the thermomechanical coupling induces a nonlinear behavior due to self-heating and self-cooling. Thus, we characterize the viscoelastic behavior of the composite by simulating DMA tests. More precisely, we run through the following steps:

1. In analogy to tensile DMA experiments, a static uniaxial tensile load of $\varepsilon_{\text{static}}$ is applied in a single step in 1 second.
2. The loading $\varepsilon_{\text{static}}$ is held constant for 100 s. In actual experiments, the holding time is usually much shorter. However, we want to mitigate the effects of the initial stress relaxation on our numerical experiments.
3. A sinusoidal loading of the form (24) with amplitude ε_{amp} and frequency f is applied over two cycles, resolved with a fixed number of load steps per cycle.
4. The amplitude σ_{amp} and the phase angle δ of the stress response (25) are determined via a least-square fit to the computed macroscopic stress values in the second cycle to avoid transient effects. Subsequently, E' and E'' are computed via Equations (26) and (27).

Note that we do not use the affine-linear extrapolation for these computations, due to the nonmonotone loading. To validate our approach and to determine the necessary number of load steps per cycle, we apply steps 1–4 for a homogeneous polypropylene microstructure under isothermal conditions. The parameters for the sinusoidal loading are $\varepsilon_{\text{static}} = 0.1\%$, $\varepsilon_{\text{amp}} = 0.05\%$, cf. Kehrer et al.,[65] and $f = 10$ Hz. For this frequency, the storage and loss modulus of the viscoelastic model for polypropylene are given by $E' = 2012.22$ MPa and $E'' = 177.68$ MPa. In addition to E' and E'', we also track the effective dissipated energy (18) in our computations and compare it to the analytical formula (28). The relative errors for E', E'' and $\mathcal{D}_{\text{cycle}}$ are shown in Figure 6 as a function of the load steps per cycle.

For more than 30 load steps per cycle, the relative error for all tracked quantities falls below 1%. Indeed, E'' as determined by our DMA computation virtually coincides with its analytical value. Note that the error in dissipation does not tend to 0 for finer resolutions. This is a consequence of the stress relaxation under static strain loading, which still causes a small additional amount of energy dissipation. In preliminary computations, a higher number of cycles was considered as well. However, the results did not differ substantially. Hence, we choose 30 load steps per cycle for all subsequent computations.

With the established procedure, we simulate uniaxial DMA tests at various static load values for the planar short glass–fiber reinforced polypropylene microstructure, see Figure 5. In particular, the effect of the thermomechanical coupling under adiabatic conditions on E' and E'' is of interest. The loading is applied in the xz-plane at angles between 0° and 90° with respect to the x-direction. Static loads $\varepsilon_{\text{static}}$ between 0.1% and 1.0% are considered. The amplitude and frequency are fixed at $\varepsilon_{\text{amp}} = 0.05\%$ and $f = 10$ Hz, respectively.

In Figure 7, the results for E' and E'' are plotted alongside the mean temperature during the harmonic excitation as a function of the loading angle. First, we take a look at the storage modulus. For the 0° load case, that is, in-plane loading, the storage modulus is at its peak value. This is due to the stiffening effect of the fibers. For increasing load angle, it drops by ca. 20% up to 45° and subsequently stagnates. Similar to the observations in Section 4.2.1, the material cools down under tensile loading due to the Gough–Joule effect, cf. Figure 7(C). This causes a stiffening of the polypropylene

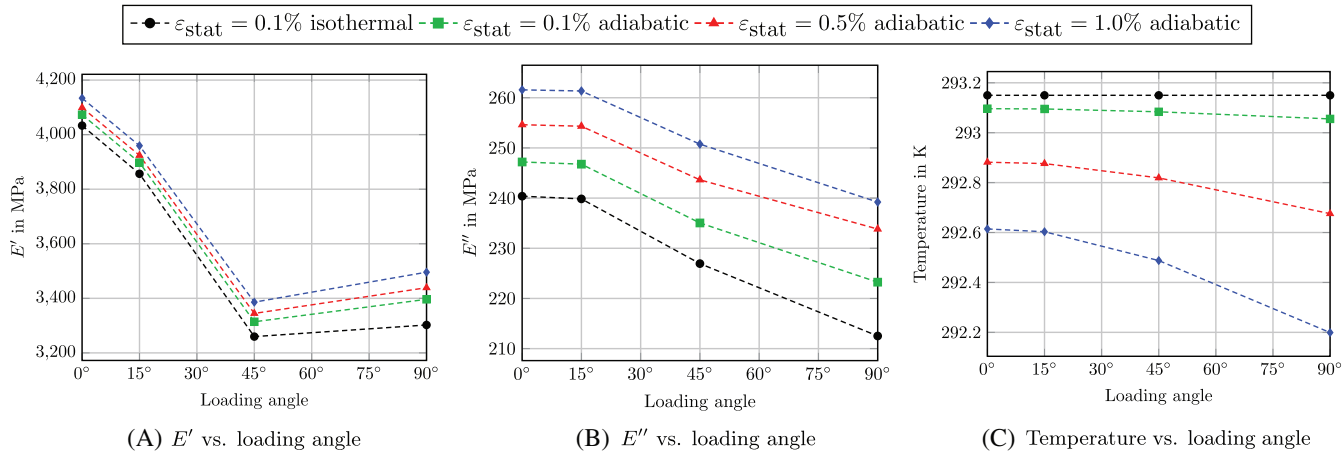

(A) E' vs. loading angle (B) E'' vs. loading angle (C) Temperature vs. loading angle

FIGURE 7 Short glass–fiber reinforced polypropylene: complex moduli and average temperature as a function of the loading angle with respect to the x-axis in the xz-plane

matrix and an increase E'. The effect is most pronounced for the 90° load case, where we observe the largest temperature difference between adiabatic and isothermal conditions. For a static load of 1.0%, the relative error between the adiabatic computation and the isothermal computation is slightly below 6%.

The loss modulus E'' displays a slightly different profile with respect to the loading angle. Its value is at its maximum between 0° to 15°, where the strong strain localization around the fibers leads to high amounts of dissipated energy. Subsequently, the loss modulus decreases linearly. The effect of the static loading on the loss modulus under adiabatic conditions is more pronounced than for the storage modulus. As a decrease in temperature brings the temperature of polypropylene closer to its glass transition temperature, the dissipated energy and E'' increase. At a load angle of 90°, where the self-cooling is most pronounced, even the lowest static loading of $\varepsilon_{static} = 0.1\%$ leads to a 5% difference in the loss moduli. The difference increases with the static loading, reaching 13% for $\varepsilon_{static} = 1.0\%$.

We conclude that the thermomechanical coupling can have a significant effect when characterizing thermoplastics-based composites using DMA. Due to the Gough–Joule effect, the effective behavior of the material, in particular E'', becomes load dependent, that is, nonlinear. This is particularly pronounced for high loading frequencies, when there is no time for thermal conduction or radiation to take place and the conditions are approximately adiabatic. To obtain precise results for real-life experiments, a strict temperature control of the specimen and low static loadings are therefore necessary.

4.3.2 | Self-heating under harmonic loading

In the previous Section 4.3.1, we considered an oscillatory loading with a small number of cycles. In this case, the observed temperature changes were mostly due to the Gough–Joule effect caused by the static loading. However, for a high number of cycles, the dissipated energy accumulates over time and becomes the main driver of the temperature evolution. For example, such conditions frequently occur in fatigue testing, where the self-heating of the specimen poses a major challenge.[2,3] Typically, in the first hundreds of cycles, the temperature increases in a roughly linear fashion[71] and subsequently reaches an equilibrium value when dissipation and thermal conduction reach an equilibrium state. This limits, for instance, the range of viable loading frequencies for testing.[72,73]

Motivated by these findings, we take a look at the effect of the thermomechanical coupling on the dissipative characteristics of the short glass–fiber reinforced composite in the initial stage of a high cycle test. More precisely, we prescribe 100 cycles of harmonic stress-controlled uniaxial tensile loading in x-direction with a frequency of $f = 10$ Hz. The static stress is fixed at $\sigma_{static} = 30$MPa with a stress amplitude of $\sigma_{amp} = 30$MPa, corresponding to a load factor of $R = \sigma_{min}/\sigma_{max} = 0$. As only a short time-frame of 10 s is considered, we assume adiabatic conditions.

First, we consider the evolution of the temperature and the strain amplitude. In Figure 8(A), the minimum, maximum, and average temperature are plotted for each cycle. Initially, the mean temperature is lower than the reference $\theta_{ref} = 293.15\ K$, due to the Gough–Joule effect. Over time, the self-heating caused by the dissipated energy leads to a linear

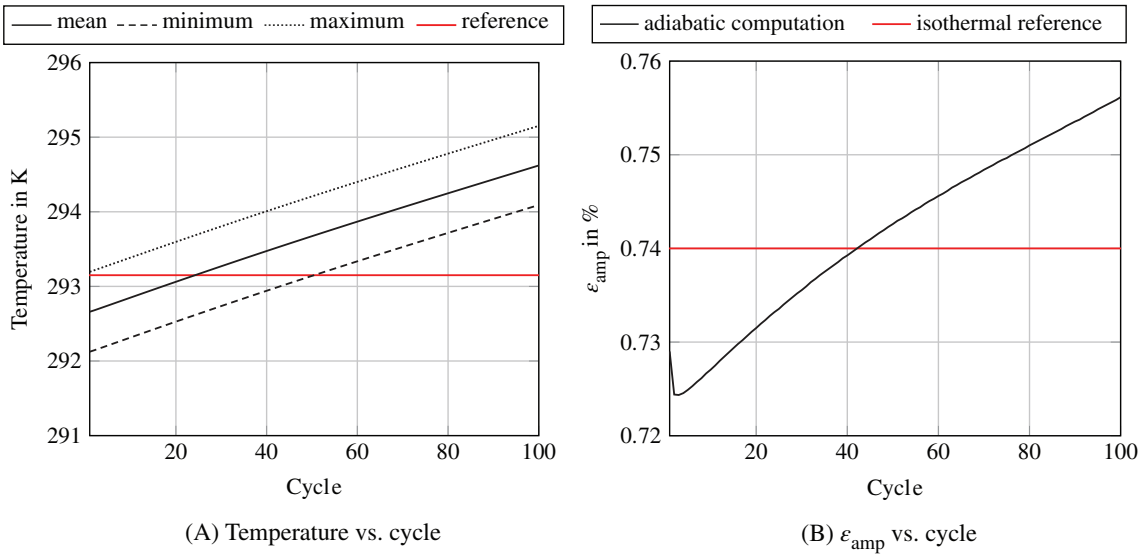

FIGURE 8 Short glass–fiber reinforced polypropylene: temperature and strain amplitude for each of 100 cycles under stress-controlled uniaxial harmonic loading in z-direction

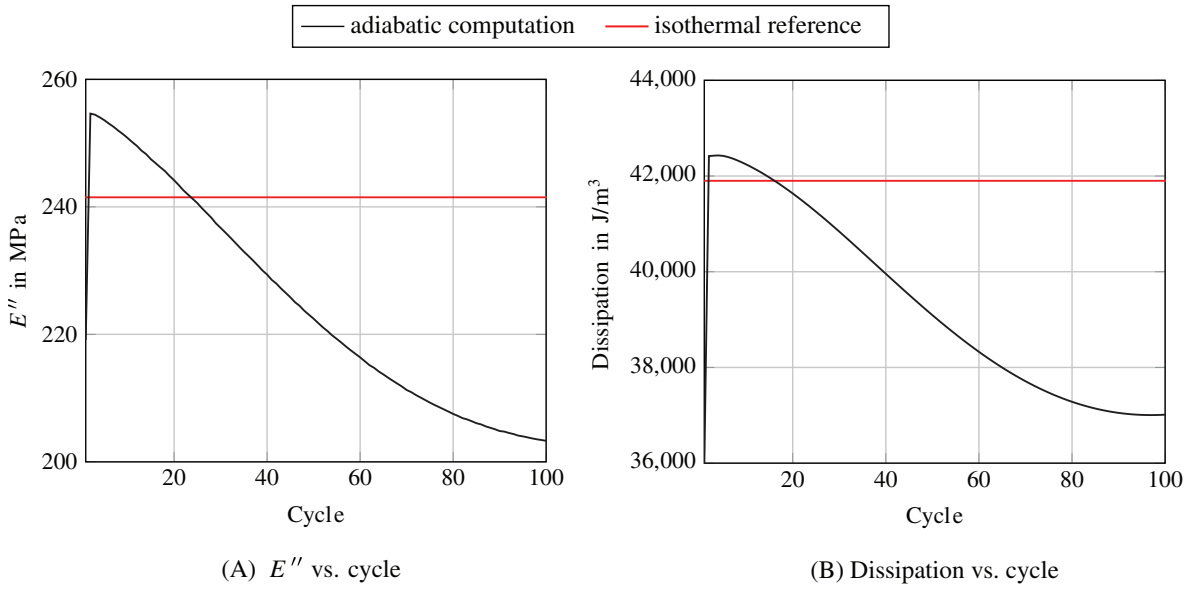

FIGURE 9 Short glass–fiber reinforced polypropylene: dissipated energy and loss modulus for each of 100 cycles under stress-controlled uniaxial harmonic loading in z-direction

increase and after 25 cycles the initial cool-down is compensated. Together with the temperature, the strain amplitude increases as the material softens, cf. Figure 8(B). However, the reference value of ε_{amp} for the isothermal case is reached after 42 cycles when the mean temperature has already surpassed θ_{ref}. Taking a look at the minimum and maximum temperature in Figure 8(A), we observe that the large stress amplitude leads to a significant fluctuation of about 1 K for each cycle. Hence, the behavior of polypropylene fluctuates within each cycle, resulting in a slight reduction of the amplitude.

Last but not least, we take a look at the dissipation and the loss modulus for each cycle. Consistent with our observations in Section 4.3.1, the magnitude of the loss modulus, cf. Figure 9(A), is initially higher than the isothermal prediction and subsequently decreases with increasing temperature. As the temperature reaches its reference value, so does E'', indicating that it is mostly unaffected by the large stress amplitude and the resulting intercyclic temperature fluctuations.

The dissipation per cycle follows a similar trend. However, it barely exceeds the isothermal reference value in the first few cycles, as the higher loss modulus is partly compensated by the lower strain amplitude.

Overall, we observe that the dissipative behavior of the material changes significantly in the first cycles of a long-term harmonic excitation. At the end of 100 cycles, the loss modulus and dissipation are 16% and 12% lower, respectively, than the values predicted for the isothermal setting. Thus, when predicting the temperature changes for fatigue tests based on (28), cf. Handa et al.,[69] accounting for the temperature dependence of the material is mandatory.

5 | CONCLUSIONS

The present study was devoted to enabling the efficient computational homogenization of thermomechanically coupled materials. Based on the consistent asymptotic homogenization framework for dissipative materials,[5] we presented an efficient staggered algorithm compatible to strain or displacement-based micromechanical solvers. Due to their computational power, we focused on FFT-based solution schemes and found that best performance was achieved in combination with the Barzilai–Borwein method. Even for a composite with strong thermomechanical coupling, its iteration counts and convergence behavior hardly differed from the usual isothermal setting. The powerful class of polarization-based schemes[19,20,74] was excluded from the present work, as the complexity-reduction approach by Schneider et al.[51] may prevent the evaluation of dissipation and entropy. Further studies are necessary, to make these solvers available for thermomechanically coupled problems.

In our numerical experiments, we observed that the computational overhead for the temperature-update step in the proposed algorithm was negligible. The difference in runtime between thermomechanically coupled and isothermal computations was dominated by evaluating the entropy and the dissipation, as part of the material law. In particular, computing the dissipation was costly for the chosen linear viscoelastic model, as it involves applying an inverse stiffness tensor for each Maxwell element. This lead to an increase in overall computation times by 20%–30%. However, for material laws such as J_2-plasticity, where the dissipation is readily computed, the difference is much smaller. Overall, we conclude that the proposed algorithm enables computing the effective mechanical behavior of thermomechanically coupled materials with nearly the same computational efficiency as traditional FFT-based methods in an isothermal setting.

For the investigated glass–fiber reinforced polypropylene composites we observed that the thermomechanical coupling induced an effectively nonlinear material behavior, even though the underlying material model was linear viscoelastic. In particular, the dissipative characteristics of the materials changed significantly between the isothermal and adiabatic computations. Expanding the study of similar polymer-based lightweight-materials, such as sheet-molding compounds,[75] to include thermal effects seems promising. The presented thermomechanical solver is compatible to the interpolation approach by Köbler et al.,[76] enabling the development of effective (macroscopic) surrogate models for arbitrary fiber orientations. For more general structures and material models, thermomechanical FFT-based computations may enter data-driven approaches, such as deep material networks,[77-79] to facilitate the simulation of components on the macroscale.

With regard to the material model of the polymer, it would be interesting to apply a free-volume-based approach for the shift factor,[63] which takes into account the pressure dependence of the viscosity. Whereas a tensile loading mechanically increases the free volume, the accompanying adiabatic cooldown, observed in this study, may weaken this effect. Investigating the interaction between these phenomena seems worthwhile to enable a thorough characterization of the thermomechanical material behavior. In addition, expanding the material model to the viscoplastic domain[57] appears attractive to investigate the influence of the plastic dissipation on the self-heating behavior of the material. As self-heating effects are particularly relevant in the context of fatigue and life-time predictions, coupling the presented thermomechanical solver with FFT-based schemes for damage[30,80] or fracture[28,29] would be of interest.

ACKNOWLEDGMENTS

The authors Daniel Wicht and Thomas Böhlke gratefully acknowledge the partial financial support by the German Research Foundation (DFG) under the project “Lamellar Fe-Al in situ composite materials” (BO 1466/12-2). The author Matti Schneider acknowledges partial financial support by the German Research Foundation (DFG) within the International Research Training Group “Integrated engineering of continuous–discontinuous long fiber reinforced polymer structures” (GRK 2078). The authors are grateful for the constructive criticism received during the reviewing process.

ORCID

Daniel Wicht https://orcid.org/0000-0002-4925-9035
Matti Schneider https://orcid.org/0000-0001-7017-3618
Thomas Böhlke https://orcid.org/0000-0001-6884-0530

REFERENCES

1. Ferry JD. *Viscoelastic Properties of Polymers*. 3rd ed. New York, NY: Wiley; 1980.
2. Rittel D. Investigation of the heat generated during cyclic loading of two glassy polymers. Part I: experimental. *Mech Mater*. 2000;32(3):131-147.
3. Mortazavian S, Fatemi A. Fatigue behavior and modeling of short fiber reinforced polymer composites: a literature review. *Int J Fatigue*. 2015;70:297-321.
4. Katunin A. Criticality of the self-heating effect in polymers and polymer matrix composites during fatigue, and their application in non-destructive testing. *Polymers*. 2019;11(1):19.
5. Chatzigeorgiou G, Charalambakis N, Chemisky Y, Meraghni F. Periodic homogenization for fully coupled thermomechanical modeling of dissipative generalized standard materials. *Int J Plast*. 2016;81:18-39.
6. Germain P, Nguyen Q, Suquet P. Continuum thermodynamics. *J Appl Mech*. 1983;50:1010-1020.
7. Terada K, Kurumatani M, Ushida T, Kikuchi N. A method of two-scale thermo-mechanical analysis for porous solids with micro-scale heat transfer. *Comput Mech*. 2010;46:269-285.
8. Temizer İ. On the asymptotic expansion treatment of two-scale finite thermoelasticity. *Int J Eng Sci*. 2012;53:74-84.
9. Charalambakis N, Chatzigeorgiou G, Chemisky Y, Meraghni F. Mathematical homogenization of inelastic dissipative materials: a survey and recent progress. *Contin Mech Thermodyn*. 2018;30:1-51.
10. Willis JR. Variational and related methods for the overall properties of composites. *Adv Appl Mech*. 1981;21:1-78.
11. Tikkarrouchine E, Chatzigeorgiou G, Chemisky Y, Meraghini F. Fully coupled thermo-viscoplastic analysis of composite structures by means of multi-scale three-dimensional finite element computations. *Int J Solids Struct*. 2019;164:120-140.
12. Özdemir I, Brekelmans WAM, Geers MGD. FE^2 computational homogenization for the thermo-mechanical analysis of heterogeneous solids. *Comput Methods Appl Mech Eng*. 2008;198(3–4):602-613.
13. Li J, Romero I, Segurado J. Development of a thermo-mechanically coupled crystal plasticity modeling framework: application to polycrystalline homogenization. *Int J Plast*. 2019;119:313-330.
14. Moulinec H, Suquet P. A numerical method for computing the overall response of nonlinear composites with complex microstructure. *Comput Methods Appl Mech Eng*. 1998;157:69-94.
15. Eisenlohr P, Diehl M, Lebensohn RA, Roters F. A spectral method solution to crystal elasto-viscoplasticity at finite strains. *Int J Plast*. 2013;46:37-53.
16. Lucarini S, Segurado J. On the accuracy of spectral solvers for micromechanics based fatigue modeling. *Comput Mech*. 2019;63:365-382.
17. Rovinelli A, Proudhon H, Lebensohn RA, Sangid MD. Assessing the reliability of fast Fourier transform-based crystal plasticity simulations of a polycrystalline material near a crack tip. *Int J Solids Struct*. 2020;184:153-166.
18. Frigo M, Johnson SG. The design and implementation of FFTW3. *Proc IEEE*. 2005;93:216-231.
19. Eyre DJ, Milton GW. A fast numerical scheme for computing the response of composites using grid refinement. *Eur Phys J Appl Phys*. 1999;6(1):41-47.
20. Michel JC, Moulinec H, Suquet P. A computational scheme for linear and non-linear composites with arbitrary phase contrast. *Int J Numer Methods Eng*. 2001;52:139-160.
21. Moulinec H, Silva F. Comparison of three accelerated FFT-based schemes for computing the mechanical response of composite materials. *Int J Numer Methods Eng*. 2014;97:960-985.
22. Gélébart L, Mondon-Cancel R. Non-linear extension of FFT-based methods accelerated by conjugate gradients to evaluate the mechanical behavior of composite materials. *Comput Mater Sci*. 2013;77:430-439.
23. Kabel M, Böhlke T, Schneider M. Efficient fixed point and Newton-Krylov solvers for FFT-based homogenization of elasticity at large deformations. *Comput Mech*. 2014;54(6):1497-1514.
24. Shantraj P, Eisenlohr P, Diehl M, Roters F. Numerically robust spectral methods for crystal plasticity simulations of heterogeneous materials. *Int J Plast*. 2015;66:31-45.
25. Schneider M. On the Barzilai-Borwein basic scheme in FFT-based computational homogenization. *Int J Numer Methods Eng*. 2019;118:482-494.
26. Wicht D, Schneider M, Böhlke T. On Quasi-Newton methods in fast Fourier transform-based micromechanics. *Int J Numer Methods Eng*. 2019;121(8):1-30.
27. Mishra N, Vondřejc J, Zeman J. A comparative study on low-memory iterative solvers for FFT-based homogenization of periodic media. *J Comput Phys*. 2016;321:151-168.
28. Chen Y, Vasiukov D, Gélébart L, Park CH. A FFT solver for variational phase-field modeling of brittle fracture. *Comput Methods Appl Mech Eng*. 2019;349:167-190.
29. Ernesti F, Schneider M, Böhlke T. Fast implicit solvers for phase-field fracture problems on heterogeneous microstructures. *Comput Methods Appl Mech Eng*. 2020;363:112793.

30. Sharma L, Peerlings RHJ, Shanthraj P, Roters F, Geers MGD. An FFT-based spectral solver for interface decohesion modelling using a gradient damage approach. *Comput Mech*. 2020;65(4):925-939.
31. Haouala S, Lucarini S, LLorca J, Segurado J. Simulation of the Hall-Petch effect in FCC polycrystals by means of strain gradient crystal plasticity and FFT homogenization. *J Mech Phys Solids*. 2020;134:103755.
32. Vidyasagar A, Tan WL, Kochmann DM. Predicting the effective response of bulk polycrystalline ferroelectric ceramics via improved spectral phase field methods. *J Mech Phys Solids*. 2017;106:133-151.
33. Chen L, Chen J, Lebensohn RA, et al. An integrated fast Fourier transform-based phase-field and crystal plasticity approach to model recrystallization of three dimensional polycrystals. *Comput Methods Appl Mech Eng*. 2015;285:829-848.
34. Vinogradov V, Milton GW. An accelerated FFT algorithm for thermoelastic and non-linear composites. *Int J Numer Methods Eng*. 2008;76(11):1678-1685.
35. Anglin BS, Lebensohn RA, Rollett AD. Validation of a numerical method based on Fast Fourier Transforms for heterogeneous thermoelastic materials by comparison with analytical solutions. *Comput Mater Sci*. 2014;87:209-217.
36. Ambos A, Willot F, Jeulin D, Trumel H. Numerical modeling of the thermal expansion of an energetic material. *Int J Solids Struct*. 2015;60–61:125-139.
37. Sixto-Camacho LM, Bravo-Castillero J, Brenner R, et al. Asymptotic homogenization of periodic thermo-magneto-electro-elastic heterogeneous media. *Comput Math Appl*. 2013;66(10):2056-2074.
38. Shantraj P, Diehl M, Eisenlohr P, Roters F, Raabe D. Spectral solvers for crystal plasticity and multi-physics simulations. In: Hsueh CH, ed. *Handbook of Mechanics of Materials*. Singapore, Asia: Springer; 2019:1347-1372.
39. Coleman BD, Noll W. The thermodynamics of elastic materials with heat conduction and viscosity. *Arch Ration Mech Anal*. 1963;13(1):167-178.
40. Stainier L, Ortiz M. Study and validation of a variational theory of thermo-mechanical coupling in finite visco-plasticity. *Int J Solids Struct*. 2010;47(5):705-715.
41. Kabel M, Fliegener S, Schneider M. Mixed boundary conditions for FFT-based homogenization at finite strains. *Comput Mech*. 2016;57(2):193-210.
42. Armero F, Simo JC. A new unconditionally stable fractional step method for non-linear coupled thermomechanical problems. *Int J Numer Methods Eng*. 1992;35:737-766.
43. Rothe S, Erbts P, Düster A, Hartmann S. Monolithic and partitioned coupling schemes for thermo-viscoplasticity. *Comput Methods Appl Mech Eng*. 2015;293:375-410.
44. Simo JC, Miehe C. Associative coupled thermoplasticity at finite strains: formulation numerical analysis and implementation. *Comput Methods Appl Mech Eng*. 1992;98:41-104.
45. Riedlbauer D, Steinmann P, Mergheim J. Thermomechanical finite element simulations of selective electron beam melting processes: performance considerations. *Comput Mech*. 2014;54(1):109-122.
46. Erbts P, Düster A. Accelerated staggered coupling schemes for problems of thermoelasticity at finite strains. *Comput Math Appl*. 2012;64(8):2408-2430.
47. Martins JMP, Neto DM, Alves JL, et al. A new staggered algorithm for thermomechanical coupled problems. *Int J Solids Struct*. 2017;122–123:42-58.
48. Vaz M Jr, Muñoz-Rojas PA, Lange MR. Damage evolution and thermal coupled effects in inelastic solids. *Int J Mech Sci*. 2011;53(5):387-398.
49. Armero F, Simo JC. A priori stability estimates and unconditionally stable product formula algorithms for nonlinear coupled thermoplasticity. *Int J Plast*. 1993;9(6):749-782.
50. Miehe C. A theory of large-strain isotropic thermoplasticity based on metric transformation tensors. *Arch Appl Mech*. 1995;66(1–2):45-64.
51. Schneider M, Wicht D, Böhlke T. On polarization-based schemes for the FFT-based computational homogenization of inelastic materials. *Comput Mech*. 2019;64(4):1-23.
52. Behnel S, Bradshaw R, Citro C, Dalcin L, Seljebotn DS, Smith K. Cython: the best of both worlds. *Comput Sci Eng*. 2011;13(2):31-39.
53. Torquato S, Jiao Y. Robust algorithm to generate a diverse class of dense disordered and ordered sphere packings via linear programming. *Phys Rev E*. 2010;82:061302.
54. Haupt P. *Continuum Mechanics and Theory of Materials*. Berlin, Heidelberg: Springer; 2002.
55. Truesdell C, Noll W. *The Non-Linear Field Theories of Mechanics*. Berlin, Heidelberg/Germany: Springer; 2004.
56. Tschoegl N. *The Phenomenological Theory of Linear Viscoelastic Behavior: An Introduction*. Berlin, Heidelberg: Springer; 1989.
57. Krairi A, Doghri I, Schalnat J, Robert G, Van Paepegem W. Thermo-mechanical coupling of a viscoelastic-viscoplastic model for thermoplastic polymers: thermodynamical derivation and experimental assessment. *Int J Plast*. 2019;115:154-177.
58. Benaarbia A, Chatzigeorgiou G, Kiefer B, Meraghni F. A fully coupled thermo-viscoelastic-viscoplastic-damage framework to study the cyclic variability of the Taylor-Quinney coefficient for semi-crystalline polymers. *Int J Mech Sci*. 2019;163:105128.
59. Tscharnuter D, Jerabek M, Major Z, Pinter G. Uniaxial nonlinear viscoelastic viscoplastic modeling of polypropylene. *Mech Time-Depend Mater*. 2012;16:275-286.
60. Warlimont H, Martienssen W, eds. *Springer Handbook of Materials Data*. 2nd ed. Cham: Springer; 2018.
61. Brinson HF, Brinson LC. *Polymer Engineering Science and Viscoelasticity*. 2nd ed. New York, NY: Springer; 2015.
62. Williams ML, Landel RF, Ferrry JD. The temperature dependence of relaxation mechanisms in amorphous polymers and other glass-forming liquids. *J Am Chem Soc*. 1955;77(14):3701-3707.
63. Fillers RW, Tschoegl NW. The effect of pressure on the mechanical properties of polymers. *Trans Soc Rheol*. 1977;21(1):51-100.

64. Taylor RL, Pister KS, Goudreau GL. Thermomechanical analysis of viscoelastic solids. *Int J Numer Methods Eng*. 1970;2:45-49.
65. Kehrer L, Wicht D, Wood JT, Böhlke T. Dynamic mechanical analysis of pure and fiber reinforced thermoset- and thermoplastic-based polymers and free volume-based viscoelastic modeling. *GAMM-Mitteilungen*. 2018;41(1):e201800007.
66. Eisenstat SC, Walker HF. Choosing the forcing terms in an inexact Newton method. *SIAM J Sci Comput*. 1996;17(1):16-32.
67. Schneider M. The sequential addition and migration method to generate representative volume elements for the homogenization of short fiber reinforced plastics. *Comput Mech*. 2017;59:247-263.
68. Advani SG, Tucker CL. The use of tensors to describe and predict fiber orientation in short fiber composites. *J Rheol*. 1987;31(8):751-784.
69. Handa K, Kato A, Narisawa I. Fatigue characteristics of a glass-fiber-reinforced polyamide. *J Appl Polym Sci*. 1999;72(13):1783-1793.
70. Esmaeillou B, Ferreira P, Bellenger V, Tcharkhtchi A. Fatigue behavior of polyamide 66/glass fiber under various kinds of applied load. *Polym Compos*. 2012;33(4):540-547.
71. Jegou L, Marco Y, Le Saux V, Calloc S. Fast prediction of the Wöhler curve from heat build-up measurements on short fiber reinforced plastic. *Int J Fatigue*. 2013;47:259-267.
72. Jia N, Kagan VA. Effects of time and temperature on the tension-tension fatigue behavior of short fiber reinforced polyamides. *Polym Compos*. 1998;19(4):408-414.
73. De Monte M, Moosbrugger E, Quaresimin M. Influence of temperature and thickness on the off-axis behaviour of short glass fibre reinforced polyamide 6.6 cyclic loading. *Compos A Appl Sci Manuf*. 2010;41(10):1368-1379.
74. Monchiet V, Bonnet G. A polarization-based FFT iterative scheme for computing the effective properties of elastic composites with arbitrary contrast. *Int J Numer Methods Eng*. 2012;89:1419-1436.
75. Görthofer J, Schneider M, Ospald F, Hrymak A, Böhlke T. Computational homogenization of sheet molding compound composites based on high fidelity representative volume elements. *Comput Mater Sci*. 2020;174:109456.
76. Köbler J, Schneider M, Ospald F, Andrä H, Müller R. Fiber orientation interpolation for the multiscale analysis of short fiber reinforced composite parts. *Comput Mech*. 2018;61(6):729-750.
77. Liu Z, Wu CT, Koishi M. A deep material network for multiscale topology learning and accelerated nonlinear modeling of heterogeneous materials. *Comput Methods Appl Mech Eng*. 2019;345:1138-1168.
78. Liu Z, Wu CT. Exploring the 3D architectures of deep material network in data-driven multiscale mechanics. *J Mech Phys Solids*. 2019;127:20-46.
79. Gajek S, Schneider M, Böhlke T. On the micromechanics of deep material networks. *J Mech Phys Solids*. 2020;142:103984.
80. Boeff M, Gutknecht F, Engels PS, Ma A, Hartmaier A. Formulation of nonlocal damage models based on spectral methods for application to complex microstructures. *Eng Fract Mech*. 2015;147:373-387.
81. Lahellec N, Suquet P. On the effective behavior of nonlinear inelastic composites: I incremental variatonal principles. *J Mech Phys Solids*. 2007;55:1932-1963.
82. Zeman J, de Geus TWJ, Vondřejc J, Peerlings RHJ, Geers MGD. A finite element perspective on non-linear FFT-based micromechanical simulations. *Int J Numer Methods Eng*. 2017;111(10):903-926.
83. Milton GW. *The Theory of Composites*. Cambridge, UK: Cambridge University Press; 2002.
84. Nesterov Y. *Introductory Lectures on Convex Optimization: A Basic Course. Mathematics and Its Applications*. Boston, MA: Kluwer Academic Publishers; 2004.
85. Barzilai J, Borwein JM. Two-point step size gradient methods. *IMA J Numer Anal*. 1988;8:141-148.
86. Dong Y. Step lengths in BFGS method for monotone gradients. *Comput Math Appl*. 2010;60(3):563-571.
87. Zeman J, Vondřejc J, Novak J, Marek I. Accelerating a FFT-based solver for numerical homogenization of periodic media by conjugate gradients. *J Comput Phys*. 2010;229(21):8065-8071.
88. Grimm-Strele H, Kabel M. Runtime optimization of a memory efficient CG solver for FFT-based homogenization: implementation details and scaling results for linear elasticity. *Comput Mech*. 2019;64(5):1339-1345.
89. Lucarini S, Segurado J. DBFFT: a displacement based FFT approach for non-linear homogenization of the mechanical behavior. *Int J Eng Sci*. 2019;144:103131.
90. Willot F. Fourier-based schemes for computing the mechanical response of composites with accurate local fields. *Comptes Rendus Mécanique*. 2015;343(3):232-245.
91. Schneider M, Ospald F, Kabel M. Computational homogenization of elasticity on a staggered grid. *Int J Numer Methods Eng*. 2016;105(9):693-720.
92. Leuschner M, Fritzen F. Fourier-accelerated nodal solvers (FANS) for homogenization problems. *Comput Mech*. 2018;32(3):359-392.
93. Schneider M, Merkert D, Kabel M. FFT-based homogenization for microstructures discretized by linear hexahedral elements. *Int J Numer Methods Eng*. 2017;109(10):1461-1489.

How to cite this article: Wicht D, Schneider M, Böhlke T. Computing the effective response of heterogeneous materials with thermomechanically coupled constituents by an implicit fast Fourier transform-based approach. *Int J Numer Methods Eng*. 2021;122:1307–1332. https://doi.org/10.1002/nme.6579

APPENDIX A. FFT-BASED SOLUTION SCHEMES FOR THE ISOTHERMAL PROBLEM

Due to their computational efficiency, we chose FFT-based algorithms for the iterative solution scheme in our staggered thermomechanical algorithm 1. In this appendix, we recast the isothermal balance of linear momentum, cf. (14), as an optimization problem. Based on this variational framework, the basic scheme,[14] the Barzilai–Borwein method,[25] and the inexact Newton method[22,23] are briefly summarized in Sections A.1–A.3.

Let $w_{\overline{\theta}}(\cdot,\varepsilon) = w(\cdot,\overline{\theta},\varepsilon)$ denote the condensed incremental potential of a generalized standard material for a fixed temperature $\overline{\theta}$, cf. Lahellec–Suquet.[81] The material law is defined by the hyperelastic relation

$$\sigma = \frac{\partial w_{\overline{\theta}}}{\partial \varepsilon}(\cdot,\varepsilon).$$

For a prescribed macroscropic strain $\overline{\varepsilon}$, we seek a compatible strain field

$$\varepsilon = \overline{\varepsilon} + \nabla^s u \quad \text{with } \langle \varepsilon \rangle_Y = \overline{\varepsilon}, \tag{A1}$$

which solves the balance of linear momentum

$$\operatorname{div} \frac{\partial w_{\overline{\theta}}}{\partial \varepsilon}(\cdot,\varepsilon) = 0. \tag{A2}$$

After solving (A2), the macroscopic stress is computed by

$$\overline{\sigma} = \left\langle \frac{\partial w_{\overline{\theta}}}{\partial \varepsilon}(\cdot,\varepsilon) \right\rangle_Y .$$

This problem can be interpreted as a critical point of the mean energy $W(\hat{\varepsilon}) = \langle w_{\overline{\theta}}(\overline{\varepsilon} + \hat{\varepsilon}) \rangle_Y$, cf., for instance, Schneider[25] or Zeman et al.,[82]

$$W(\hat{\varepsilon}) \to \min_{\hat{\varepsilon} \in U \subset V}$$

with respect to the strain fluctuations $\hat{\varepsilon}$ in the subspace

$$U = \{\hat{\varepsilon} \in V | \hat{\varepsilon} = \nabla^s u, u \in H^1_{\#}(Y, \mathbb{R}^d)\},$$

where $H^1_{\#}(Y,\mathbb{R}^d)$ denotes the first-order Sobolev space of periodic and mean-free displacement fluctuations u. By the Helmholtz decomposition, cf. chapter 12.1 in Milton's book,[83] $\Gamma = \nabla^s(\operatorname{div} \nabla^s)^{-1}\operatorname{div}$ is an orthogonal projector onto U. Thus, we can write the differential in the form

$$DW(\hat{\varepsilon})[S] = \left\langle \Gamma : \frac{\partial w_{\overline{\theta}}}{\partial \varepsilon}(\overline{\varepsilon} + \hat{\varepsilon}), S \right\rangle_{L^2}, \quad S \in U$$

and identify the gradient

$$\nabla W = \Gamma : \frac{\partial w_{\overline{\theta}}}{\partial \hat{\varepsilon}}(\cdot,\varepsilon).$$

by the definition

$$\langle \nabla W(\hat{\varepsilon}), S \rangle_{L^2} = DW(\varepsilon)[S], \quad \forall S \in U.$$

Note that the condition $\nabla W = 0$ for critical points of W is equivalent to the static equilibrium $\operatorname{div} \sigma = 0$ in (A2).

A.1 Basic scheme

Using the gradient descent method for solving (A2) yields the iterative scheme[23]

$$\varepsilon_{k+1} = \varepsilon_k - s_k \Gamma : \frac{\partial w_{\overline{\theta}}}{\partial \varepsilon}(\cdot,\varepsilon_k). \tag{A3}$$

The optimal step size for the scheme is given by

$$s = \frac{2}{\beta^+ + \beta^-}, \tag{A4}$$

cf. section 1.2.3. in Nesterov's book,[84] where β^+ and β^- denote the extreme eigenvalues of the material tangent $\frac{\partial^2 w_{\bar{\theta}}}{\partial \varepsilon^2}$ evaluated over all microscopic points. Rewriting (A3) as a Lippmann–Schwinger equation

$$\varepsilon_{k+1} = \bar{\varepsilon} - \Gamma^0 : \left(\frac{\partial w_{\bar{\theta}}}{\partial \varepsilon}(\cdot, \varepsilon_k) - \mathbb{C}^0 : \varepsilon_k \right), \quad \text{with} \quad \mathbb{C}^0 = \frac{1}{s}\mathrm{Id}, \quad \text{and} \quad \Gamma^0 = s\Gamma,$$

we see that the gradient-descent method coincides with Moulinec–Suquet's basic scheme.[14] The pseudocode for the basic scheme is summarized in Algorithm 2.

Algorithm 2. Basic scheme iteration$(\varepsilon, \bar{\varepsilon}, s)$[14]

1: $\varepsilon \leftarrow \frac{\partial w_{\bar{\theta}}}{\partial \varepsilon}(\varepsilon) - \mathbb{C}^0 : \varepsilon$
2: $\varepsilon \leftarrow \mathrm{FFT}(\varepsilon)$
3: $\varepsilon(\xi) \leftarrow \begin{cases} \bar{\varepsilon} & \xi = 0 \\ -\Gamma^0(\xi) : \varepsilon(\xi) & \text{else} \end{cases}$
4: $\varepsilon \leftarrow \mathrm{FFT}^{-1}(\varepsilon)$
5: return ε

The basic scheme is robust and memory efficient as it operates on a single strain-like field. However, it converges exceedingly slow for composites with high material contrast $\kappa = \beta^+/\beta^-$.

A.2 Barzilai–Borwein method

Schneider[25] exploited the quasi-Newton-based Barzilai–Borwein[85] step size for gradient descent

$$s_k = s_{k-1}\left(1 - \frac{\langle \frac{\partial w_{\bar{\theta}}}{\partial \varepsilon}(\cdot, \varepsilon_k), \Gamma : \frac{\partial w_{\bar{\theta}}}{\partial \varepsilon}(\cdot, \varepsilon_{k-1})\rangle_{L^2}}{\|\Gamma : \frac{\partial w_{\bar{\theta}}}{\partial \varepsilon}(\cdot, \varepsilon_{k-1})\|_{L^2}}\right)^{-1} \quad \text{with} \quad s_0 = \frac{2}{\beta^+ + \beta^-}, \tag{A5}$$

to accelerate the basic scheme (A3). The resulting algorithm is presented in Algorithm 3 and requires storing two strain-like fields. Note that for the first iteration ($k = 0$), a single iteration of the basic scheme, cf. Algorithm 2, should be used to fix the mean value of ε.

Algorithm 3. Barzilai–Borwein iteration$(\varepsilon, \bar{\varepsilon}, s)$[25]

1: $\begin{bmatrix} R \\ \text{innerProduct} \end{bmatrix} \leftarrow \begin{bmatrix} \frac{\partial w_{\bar{\theta}}}{\partial \varepsilon}(\varepsilon) \\ \left\langle \frac{\partial w_{\bar{\theta}}}{\partial \varepsilon}(\varepsilon) : R \right\rangle_Y \end{bmatrix}$
2: $R \leftarrow \mathrm{FFT}(R)$
3: $R(\xi) \leftarrow \begin{cases} 0 & \xi = 0 \\ -\Gamma(\xi) : R(\xi) & \text{else} \end{cases}$
4: $R \leftarrow \mathrm{FFT}^{-1}(R)$
5: $s \leftarrow s/(1 - \text{innerProduct}/\|R\|_{L^2})$
6: $\varepsilon \leftarrow \varepsilon - sR$
7: return ε

In practice, the Barzilai–Borwein method outperforms the basic scheme significantly, both in terms of iteration count and runtime.[25,26] For problems where the computational effort of evaluating $\sigma = \frac{\partial w_{\bar{\theta}}}{\partial \varepsilon}(\varepsilon)$ is comparable to the cost of

computing Γ and the associated FFTs, the Barzilai–Borwein method is the general-purpose method of choice. Note, however, that its convergence behavior is nonmonotone.

A.3 Inexact Newton method

The inexact Newton method in conjunction with Krylov-subspace solvers was introduced to FFT-based micromechanics by Gélébart–Mondon–Cancel[22] and Kabel et al.[23] A Newton iteration for solving (A2) reads

$$\varepsilon_{k+1} = \varepsilon_k + \alpha_k \Xi_k, \tag{A6}$$

where the damping parameter $\alpha_k \in (0, 1]$ is determined by an inexact line-search[86] and Ξ_k solves

$$\Xi_k + \Gamma^0 : \left[\frac{\partial^2 w_{\overline{\theta}}}{\partial \varepsilon^2}(\cdot, \varepsilon_k) - \mathbb{C}^0 \right] : \Xi_k = -\Gamma^0 : \frac{\partial w_{\overline{\theta}}}{\partial \varepsilon}(\cdot, \varepsilon_k), \tag{A7}$$

up to a prescribed tolerance γ_k. In our implementation, we rely upon Dong's criteria[86] to determine α_k and use Eisenstat–Walker's choice 2[66] for γ_k. For an algorithmic overview, see Algorithm 4. The conjugate-gradient (CG) method is very efficient for solving (A7). Zeman et al.[87] showed that the CG method is independent of s entering the reference material $\mathbb{C}^0$. As it does not matter, we use the step size of the basic scheme (A4). More precisely, we start with a single iteration of the basic scheme to fix the mean value of ε and $\mathbb{C}^0$.

Algorithm 4. Newton iteration with Dong's line search[86] $(\varepsilon, \overline{\varepsilon}, s, c_{1,0}, c_2, \text{maxit})$

```
Ξ ← −( Id + Γ^0 : [ ∂²w_θ̄/∂ε² (ε) − C^0 ] )^−1 : Γ^0 : ∂w_θ̄/∂ε (ε)      ▷ Solving (A7), cf. Kabel et al.[23]
μ ← 0
ν ← +∞
α ← 1
k ← 0
while k<maxit do
    k ← k + 1
    c_1 ← c_{1,0}(1 − (c_2)^k) − (c_2)^k      ▷ Typical line-search parameters: c_{1,0} = 10^−4, c_2 = 0.9, cf. Dong[86]
    if ⟨Γ^0 : ∂w_θ̄/∂ε (ε + αΞ), Ξ⟩_{L²} > c_1 ⟨Γ^0 : ∂w_θ̄/∂ε (ε), Ξ⟩_{L²} then
        ν ← α
        α ← 0.5(μ + ν)
    else if ⟨Γ^0 : ∂w_θ̄/∂ε (ε + αΞ), Ξ⟩_{L²} < c_2 ⟨Γ^0 : ∂w_θ̄/∂ε (ε), Ξ⟩_{L²} then
        μ ← α
        α ← 2μ
    else
        break
    end if
end while
ε ← ε + αΞ
return ε
```

Newton's method exhibits excellent performance, especially for composites where the evaluation of the material law dominates the overall runtime. However, its memory requirements are significant. If CG is used for solving (A7) and the tangent is kept in memory, 8.5 strain-like fields have to be stored. Using Dong's line search increases the memory requirements by an additional strain field.

Memory efficient versions of the Newton–CG method[23,88,89] operating on the displacement instead of the strain can be implemented, provided a finite-difference[90,91] or a finite-element[92,93] discretization is used. Additional memory can be saved by storing the Hessian in single precision,[26] resulting in a reduced memory footprint of nine displacement fields.